Trapping and Laser Cooling Calcium Ions

Rudy Echavarría

Advisor: Professor David Hanneke
May 7, 2026

Submitted to the
Department of Physics & Astronomy of Amherst College
in partial fulfilment of the
requirements for the degree of
Bachelors of Arts with honors

Abstract

Ion trapping serves as an invaluable technique for studying the quantum states of atoms and molecules. By ionizing and trapping particles with dynamic electric fields, we can localize them in space and isolate them from their environment. From here, they can be addressed with lasers to manipulate their quantum states, which makes them great probes for new physics. One experiment enabled by this work is the search for potential drifts in the proton-to-electron mass ratio, μ, through studying the vibrational transitions of the oxygen molecular ion. Drifts in this transition over time would indicate time dependence in μ–currently understood as a fundamental constant–and thus, the presence of dark matter or quantum gravity. A key component of this experiment is a co-trapped atomic ion species, which sympathetically cools the motion of the oxygen molecules. Previously, the Hanneke Lab successfully co-trapped beryllium atoms with oxygen molecules, but it became of interest to co-trap oxygen with calcium instead, due to calcium's larger mass, which provides more favorable dynamics in the trap. This thesis project consists of taking a functional ion trap system for beryllium and oxygen and making it suitable for calcium and oxygen. To do so, we designed, built, and laid out the mechanical and optical systems to allow for the trapping and cooling of $^{40}Ca^{+}$. This included building and installing a calcium oven, as well as designing and laying out a four-laser system to eventually laser cool $^{40}Ca^{+}$. This four-laser system involves 423 nm and 375 nm lasers for photoionizing neutral calcium, as well as 397 nm and 866 nm lasers for cooling ionized calcium. Ultimately, we successfully ionized, trapped, cooled, and imaged calcium ions in crystallized form. We also tested different trap parameters for our linear Paul trap and examined how the ion crystal's shape responded. The Hanneke Lab now has a functional ion trap system that has the tools to trap calcium and oxygen together to measure the vibrational transition of oxygen.

Acknowledgments

I would like to thank Professor Hanneke for his guidance and support as my academic advisor, thesis advisor, and mentor over the past few years. Being able to contribute to his research has been such a rewarding experience, and his constant support and knowledge helped me immensely during this process. I would also like to thank Dr. Shylla for her guidance during this thesis project in the Hanneke Lab. Thank you to James Kubasek for his assistance in the machine shop and constant positive energy. Thank you to my professors in the Physics and Astronomy Department for providing me with an incredible education. Thank you to my fellow physics majors and Hanneke Lab mates for creating a supportive environment throughout the thesis process and my four years through the major.

This thesis is based upon work supported by the Amherst College Provost and Dean of the Faculty and by the National Science Foundation under grant PHY-2207623 (RUI PM).

Contents

List of Figures

Chapter 1

Introduction

Ion trapping techniques offer a window into new physics, new technology, and thus, into the future. By confining charged atoms or molecules in dynamic electric fields, fundamental physics constants can be tested and same-species qubits can be studied for the development of quantum computing. This thesis project took an already working ion trap apparatus—designed for $^{9}Be^{+}$ atoms and $^{16}O_2^{+}$ molecules—and made it suitable for $^{40}Ca^{+}$ and $^{16}O_2^{+}$ trapping. While the Hanneke Lab is on the hunt for new physics, motivations for this work also derive from the development of optical-frequency, metastable-state, and ground-state qubits in the field of trapped-ion quantum computing.

1.1 Ion Traps

Ion traps in ultra-high vacuum create an ideal environment to confine particles in space. The positions of the trapped particles are known, and they are shielded from background gases. From here, the quantum states of the trapped particles can be manipulated and studied. These particles can be atoms or molecules. For atomic and molecular ions, since they are charged, their spatial position can be manipulated by electric fields. If such an electric field is applied so that a particle is confined within a small volume, it can be addressed, manipulated, and studied using lasers.

According to Earnshaw's Theorem, charged particles cannot be confined in space by using solely electrostatic forces. To circumvent this issue, dynamic electric fields become of interest. By using a sinusoidally oscillating field in one plane while maintaining a constant voltage along an orthogonal axis, charged particles can effectively be trapped in space [1]. The development of the linear Paul trap is immensely important in Atomic, Molecular, and Optical physics. More detail on the dynamics of the linear Paul trap will be provided in Sec 2.2. This chapter will first build an intuition for quantum computing to motivate how ion traps are useful for applications beyond fundamental physics experiments. This chapter will then explain how ion traps are crucial to fundamental physics experiments, the goals of the Hanneke Lab, and this thesis project.

1.2 Quantum Computing

Classical computers hold information and execute tasks through the use of bits and gates. Bits are where information is stored, taking values of 0 and 1 (known as the binary digits) [2, 3]. In computer hardware, this bit can take the physical form of a transistor, where the absence of an electrical current through a wire represents a 0 bit (off) and the presence of such a current represents a 1 bit (on) [3]. For bits to be useful, they must change or react according to a presented task. Classical logic gates take advantage of bits, having two inputs and one output. These gates include OR, AND, NOT, and NAND, all common logical statements in mathematical logic [3].

Richard Feynman considered the possibility of quantum mechanical computers that could simulate any physical system [4]. Quantum computers take advantage of quantum mechanics, where wave-particle duality and other non-classical phenomena exist [3]. They operate with quantum bits, known as qubits, which have two states as well, $|0\rangle$ and $|1\rangle$. However, qubits have the ability to be in a superposition of states.

In short, quantum computers have greater computing and processing power than classical

computers. A qubit's state can now be represented in the following form:

$$|\psi\rangle = \alpha|0\rangle + \beta|1\rangle$$

where

$$|\alpha|^2 + |\beta|^2 = 1$$

and α and β are complex numbers. $|\alpha|^2$ is the probability of a qubit being in the $|0\rangle$ state, and $|\beta|^2$ is the probability of a qubit being in the $|1\rangle$ state.

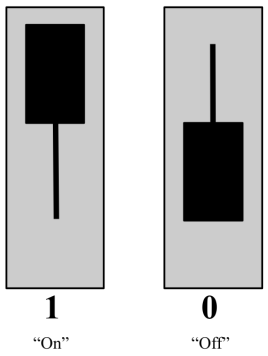

Figure 1.1: Classical bit modeled by a light switch with no dimming features.

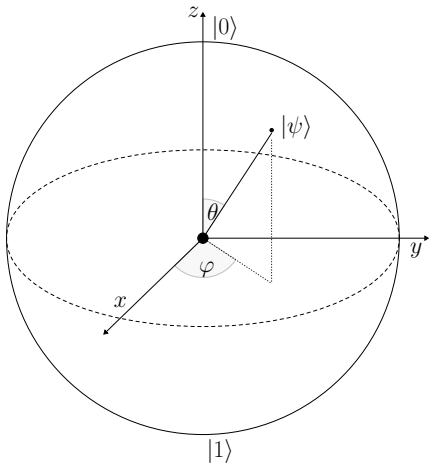

Figure 1.2: Quantum bit modeled by the Bloch Sphere.

This phenomenom can be modeled by the Bloch sphere in Figure 1.2. Every point on its surface except the poles represents some superposition of the $|0\rangle$ and $|1\rangle$ basis states. The qubit's state can be modeled as a unit vector on this two-dimensional complex vector space with two orthonormal basis vectors: $|0\rangle$ and $|1\rangle$ [5]. Generally, the qubit's state can be expressed on the Bloch sphere as

$$|\psi\rangle = \cos\frac{\theta}{2}|0\rangle + e^{i\phi}\sin\frac{\theta}{2}|1\rangle.$$

Readout of a quantum state, as with any measurement of a quantum system, collapses the wavefunction to one of the basis states, and it is not possible to get continuous data out. Other tasks involved with quantum computing are quantum state preparation, quantum gate operations, read out, quantum error-correction, etc. Generally, the quantum advantage can be understood in the fact that the classical world, ruled by Newtonian mechanics, is a special limit of quantum mechanics [6]. Simulating and completing tasks through quantum computers should then have much greater computational power than classical computers.

Now, we are left with a couple questions: how can a quantum computer be realized? What physical system can create a good environment for quantum information and processing?

According to David P. DiVincenzo, there are five criteria in determining whether or not a system can serve as an effective quantum processor [6]:

1. The system needs a collection of two-level qubits.

2. The system needs to be able to initialize each qubit into an easily referenceable state, as registers should be at a known value before computation.

3. The system needs to be able to have gate times much shorter than decoherence times (decoherence times characterize how the qubits in a system interact with its environment and represent the decay of the superposition of states).

4. The system needs a universal set of gates, similar to the OR, AND, NOT, and NAND

gates of classical systems [3].

5. The system needs to be capable of accurately measuring the qubit state.

1.2.1 Atomic Ions as Qubits

Trapped atomic ions show much promise as a candidate for qubits. Atoms are everywhere. They can be made readily available, and if they are from the same species and isotope, they will have the same structure and properties [7]. A common choice of atom for such tasks is an atom in Group-II, mainly for their relatively simple level structures with cycling transitions, since they have only one valence electron after ionization.

With respect to DiVincenzo's criteria, trapped atomic ions pass with flying colors. The system has a collection of two-level qubits, with their internal electronic states as the $|0\rangle$ and $|1\rangle$ qubit states [7]. Initialization into an easily referenceable state can be achieved through exciting an ion to one of its excited states via a laser. The ion may decay into a state that does not get excited by the frequency of the laser. The ion will then will then remain in that state. This process, called optical pumping, eventually ensures the ion is in one of its qubit states. In the case of $^{40}Ca^{+}$, the $|0\rangle$ state could be the $3D_{5/2}$ metastable state, and the $|1\rangle$ state could be the $4S_{1/2}$ ground state (see Figure 3.9 for a full picture). This is simply one possible type of qubit, known as the optical qubit.

Universal and high-fidelity gates have been demonstrated with trapped atomic ion qubits, with coherence times much longer than gate times, satisfying DiVincenzo's third criteria [7]. These operations can be achieved by applying laser or microwave drives of different frequencies to the ions. Finally, their readout follows a simple process of coupling the $|1\rangle$ state to a transition via a resonant laser and ensuring no coupling to the $|0\rangle$ state. The transition, called a cycling transition, will scatter many photons in processes described in Chapter 3, and the $|0\rangle$ state remains in the dark, making it clear what state the qubit is in [7].

The process of laser cooling also proves to be crucial in state preparation for a two-

qubit-gate, which involves the shared motional modes of ions [7]. Laser cooling combats the heating of the ions' motional modes (described in further detail in Section 3), but in this process many photons get emitted, causing decoherence of the qubits. Due to this, cooling cannot be done on data qubits, so a separate species of atomic ions can be introduced to sympathetically cool the data qubits. These ions will not store information. Using this solution, significant energy differences between transitions in both species shield information qubits from emitted light of coolant ions. This is known as dual-species ion trapping [7]. However, trapping multiple species of ions together causes a few issues such as (but not limited to) [8]:

- Requirement of twice as many stabilizing lasers.
- Difficulties cooling all of the shared motional modes.
- Different species coupling differently to stray fields.

1.2.2 *omg* Architecture

In 2021, a new blueprint proposed a potential solution, using the benefits of dual-species ion trapping and the simplicity of trapping ions of a single species [8]. This solution involves using a single atomic species and takes advantage of three different electronic qubits afforded by Group-II elements. The three electronic qubits, optical-frequency (o), metastable-state state (m), and ground-state (g), can all be addressed to perform necessary tasks without affecting the other.

Optical-Frequency (o): One ground state, one metastable state, and an energy splitting with an optical frequency. This is the qubit previously discussed.

Metastable-State (m): Two metastable atomic states, either as hyperfine splitting or Zeeman states. Zeeman states appear when the ions are placed in a magnetic field, and degenerate states respond by splitting into different energy levels, scaled by the strength of the magnetic field.

Ground-State (g): Two long-lived atomic ground states, either as hyperfine splittings or Zeeman states. Hyperfine splittings occur due to interactions between the nuclear magnetic moment and the electronic magnetic moments [9].

This solution bears the name of the *omg* architecture. Since the *omg* architecture only requires a single species of atoms, laser cooling becomes more efficient, all ions respond to the dynamic field similarly, the impact from stray fields diminishes, the number of lasers and optical components reduces, and only one species of atom needs to be loaded and trapped [8].

Different combinations of these qubits can work as the state preparation, gate, storage, and readout functions of a quantum operation. Note that these processes require much more complex and thoughtful engineering, but I will leave the discussion of trapped-ion quantum computing until Chapter 5.

1.3 Searches for New Physics

While quantum information is an applied field that uses ion-trapping techniques, many of the same techniques are used for precision measurements and probes for new physics.

1.3.1 Atomic Clocks

The use of trapped atomic ions as qubits derived from the development of atomic clocks [7]. In general, clocks operate via a regular, periodic event. This event occurs at a constant frequency and serves as a stable time reference. Atoms make ideal systems as frequency standards, as they are naturally occurring, abundant, and have two quantum states that correspond to one of its natural oscillations [10]. For example, the Systeme International (SI) unit for the second, is the defined by an atomic transition [11].

1.3.2 Standard Model

The Standard Model of particle physics is the most accurate and successful model in terms of understanding, explaining, and predicting many phenomena in different fields of physics [12]. However, it is not perfect. It cannot explain and predict the observed difference in matter and antimatter, and it cannot provide the framework for combining gravity with its own fundamental interactions [12]. While attempts to search for new particles can occur at the high-energy particle physics level by the use of a large scale collider, new physics can also be found using low-energy precision measurements. Thus, techniques such as those involved with clocks can be used to probe for new physics.

1.3.3 Fundamental Constants

Fundamental constants are parameters that are not defined by the theories they appear in. This means that fundamental constants are not predicted values, rather measured values [13]. Two examples of fundamental constants include:

$$\alpha = \frac{1}{4\pi\epsilon_0}\frac{e^2}{\hbar c}, \tag{1.1}$$

the fine structure constant, and

$$\mu = \frac{m_p}{m_e}, \tag{1.2}$$

which is the proton-to-electron mass ratio. The fine structure constant defines the strength of the electromagnetic interaction.

Certain theories propose the idea that these fundamental constants are not actually constants, rather dynamic fields [12]. Amongst these theories are discrete quantum gravity and dark matter [14, 15]. The possibility of the variation of fundamental constants can be addressed via studying atomic and molecular clocks, which have become crucial for these

searches due to their high precision.

Molecular spectroscopy offers more opportunities to monitoring these constants. Molecules, which are multiple-atom systems, allow for the atoms to vibrate and rotate with respect to one another. These added degrees of freedom lead to more energy levels, known as the rovibrational states, and they have spectra filled with many transitions. If the proton-to-electron mass ratio is spacetime dependent, so are atomic and molecular spectra [12].

If fundamental constants are found to be dynamical, then it means there is new physics that has not yet been postulated [16]. Thus, the bounds of knowledge can be pushed.

1.4 Searches for drifts in μ

In the Hanneke Lab, we hope to search for drifts in μ through the vibrational transitions of diatomic molecules. As previously stated, molecules have more degrees of freedom than atoms, so they have more energy levels. A good way to probe for drifts is to find two states which respond differently to μ,

$$hf = E'(\mu) - E''(\mu), \tag{1.3}$$

and we can monitor the frequency f of the energy difference, where h is Planck's constant. Any shift in f can be related to a fractional change in μ [17].

A diatomic molecule can be modeled by two masses on a spring, or more specifically, the harmonic oscillator. Since m_p governs the total mass at the ends of the spring, and m_e governs the chemical bond (which serves as the spring constant), it intuitively follows that a drift in m_p/m_e would change the vibrational frequency of a diatomic molecule. A more quantitative approach is provided below, following the derivation in [18].

In quantum mechanics, one can use the harmonic oscillator potential and solve for the eigen-energy levels [19]:

$$E_n = hf_o(v + \frac{1}{2}). \tag{1.4}$$

In Equation 1.4, f_o is the oscillation frequency of the diatomic molecules, v is the vibrational quantum number given in integer steps, and h is Planck's constant. However, in the Hanneke Lab, we like to write the harmonic vibrational energy in units of wavenumber– cm^{-1}. Looking at just the vibrational energy of a diatomic molecule, we can express it in units of wavenumber:

$$\frac{E}{hc} = \omega_e(v + \frac{1}{2}) \tag{1.5}$$

and

$$\omega_e = \frac{f_o}{c} = \frac{1}{2\pi c}\sqrt{\frac{k}{m}}. \tag{1.6}$$

In Equation 1.6, k is the spring constant of the oscillation, c is the speed of light, and m is the reduced mass of two indentical nuclei. Note that there are other energies associated with diatomic molecules, but since vibrational transitions hold the highest sensitivity constant and vibrational transitions are the simplest to drive, we focus on the vibrational energy. More detail and description of the sensitivity constant can be found in [17]. Since k is proportional to the mass of the electron, m_e, and the reduced mass m is proportional to the mass of the proton, m_p, we can make the relation

$$E \propto \omega_e \propto \sqrt{\frac{m_e}{m_p}} = \frac{1}{\sqrt{\mu}}. \tag{1.7}$$

Ultimately, we can relate the difference in energy from Equation 1.3 to a fractional change in μ, related by an absolute sensitivity factor c_μ. This can expressed, from [15], by

$$\Delta E = c_\mu \frac{\Delta\mu}{\mu}. \tag{1.8}$$

Our molecule of choice is $^{16}O_2^+$, and we study the $v = 0$ to $v = 16$ vibrational transition.

1.5 Experimental Setup

To probe for drifts in μ, the Hanneke Lab uses dual-species ions in a linear Paul trap, operated in ultra-high vacuum. Linear Paul traps, which will be discussed in detail in Chapter 2, apply a quadrupolar field that oscillates at a radiofrequency (RF) in one plane and a static field along an orthogonal axis. We use the linear Paul trap designed by former thesis student Shenglan Qiao, which is known as the Qiao Trap [20]. The trap is made up of what looks like four electrodes, but in reality is 12, since two of the electrodes are segmented into five subelectrodes. The segmented electrodes provide the static potential along the trap's axis.

To probe for drifts in μ, we use $^{16}O_2^+$ molecules, due to their electric dipole forbidden transition with high sensitivity to shifts in μ, as explained in Section 1.4. O_2 molecules get introduced through a molecular beam, and they get ionized through a laser process called 2+1 resonance enhanced multi-photon ionization (REMPI) via a 301 nm pulsed laser. To cool the molecules, we introduce an atomic species into the trap through an oven and a photoionization process. Then, we can laser cool the atomic ions in order to sympathetically cool the $^{16}O_2^+$ molecules. The cooling process also fluoresces the coolant atoms, so it allows us to see the amount of ions in the trap, where the coolant atoms appear bright and $^{16}O_2^+$ appear dark. Then, we will drive the vibrational transition of $^{16}O_2^+$ via a 767.6 nm laser to its 16th excited vibrational state. Next, we will apply a 355 nm laser, which will split the molecule apart into two atoms only if the molecule is already in its 16th excited state. From there, we can employ tricks in the RF trap (explained in Section 5.2) to test to see if there are O^+ atoms inside of the trap. This will allow us to see if we successfully drove the transition from $v = 0$ to $v = 16$. From here, we can track the frequency at which we drove the transition, and perform this measurement over the course of a year and test for drifts.

To prevent background gases from interfering with the trapped particles, we operate our

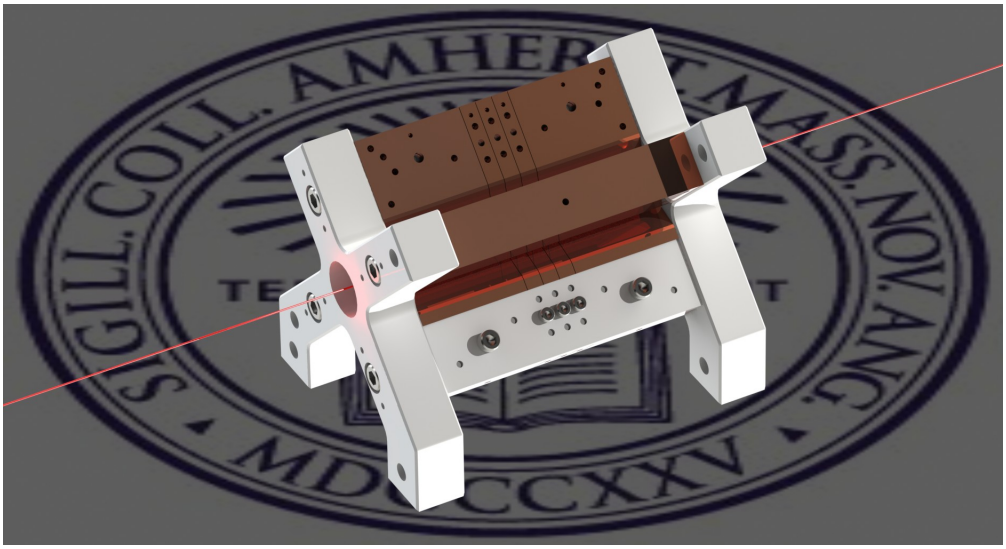

Figure 1.3: Qiao Trap modeled on SOLIDWORKS with laser propagating along trap axis (Credit: James Kubasek).

trap at ultra-high vacuum. Our vacuum chamber has seven viewports, six along the sides so that lasers can be propagated through the trap, and one larger viewport on the top so that we can image the ions. The lasers are all tuned, monitored, modulated, and stabilized in separate parts of the lab and fiber coupled to the trap.

1.6 Upgrades

The Hanneke Lab had a set-up suitable for driving the transitions of $^{16}O_2^+$ and had previously state-selectively ionized $^{16}O_2^+$. $^9Be^+$ was used to sympathetically cool the $^{16}O_2^+$. However, it became of interest to cool with an ion of a heavier mass: $^{40}Ca^+$. Using $^{40}Ca^+$ provides more ideal dynamics in the trap when it is cooled to an ionic crystal structure. A heavier coolant ion, like $^{40}Ca^+$, leads to a trapped crystal structure in which the coolant ion forms around the target ion ($^{16}O_2^+$). Using $^{40}Ca^+$ provides the following benefits:

- There is more effective laser cooling due to closer proximity between the different species.

- It will be easier to detect and count $^{16}O_2^+$ since they will appear as a dark core in fluorescing $^{40}Ca^+$ formation.
- $^{16}O_2^+$ will form closer to the axis and will see a more uniform beam.
- The lasers associated with the transitions of $^{40}Ca^+$ are much easier to use than those for Be^+.

These reasons will be further developed in Section 3.2.

For the process of laser cooling, beryllium got introduced into the trap chamber by running current through an oven in a mount attached to the base of the chamber, just in front of the trap. They were then ionized to Be^+ by laser-induced transitions, with similar techniques applied to achieve laser cooling. Upgrading the trap to be suitable for ^{40}Ca requires some new mechanical and optical systems:

- A way to load calcium into the chamber, or in other words, a functional calcium oven.
- A photoionization laser system to ionize ^{40}Ca. This includes a 423 nm resonant transition to excite ^{40}Ca and a 375 nm laser which ionizes ^{40}Ca.
- Laser systems for laser cooling. These include a 397 nm laser for the Doppler cooling transition and a 866 nm laser to repump any ions stuck in a metastable state of $^{40}Ca^+$.

The laser systems involve much more than what was mentioned, as they must be tuned, modulated, and stabilized according to our needs. More details on this will be given in Chapter 3. In short, this project aims at switching the co-trapped atomic ions from Be^+ to Ca^+, due to the more desirable features of Ca^+ when co-trapped into an ion-crystal with O_2^+.

Now, why even go over the *omg* architecture solution if this project's goal is to develop a new dual-species trap? Well, the answer is that the *omg* architecture is a recent a development in a field that uses much of the same techniques we use, and the application of the *omg* architecture could be an exciting development in an already exciting and rapidly growing

field. Ion trapping techniques are not just limited to fundamental physics experiments, they also are one of the leading techniques in the development of quantum technologies.

The next chapters will discuss in detail the mechanisms related to this project and how they relate to the ultimate goal of measuring drifts in μ. In Chapter 2, I will discuss the theory behind RF traps, our trap set-up, our RF circuit, the vacuum chamber, and our oven upgrade. Then, in Chapter 3, I will develop the atomic theory necessary to understand the transitions we drive in ^{40}Ca, as well as the optical components that allow us to tune, monitor, modulate, and stabilize the laser frequencies. In Chapter 4, I will show how we successfully trapped $^{40}Ca^{+}$ into a Coulomb crystal form and discuss how we can change its position through the adjustment of DC and dynamical voltages in the Qiao Trap. Finally, I conclude by tying all of the work back to the ultimate goal of measuring drifts in μ, what steps are left to achieve that goal, and a brief discussion tying the work to trapped-ion quantum computing.

Chapter 2

Radiofrequency Traps

In order to conduct fundamental experiments that probe for drifts in the proton-to-electron mass ratio, we must confine atoms and molecules together. In this chapter, I will discuss the mechanical systems that trap charged particles in three-dimensional space. I will start with the theory of the linear Paul trap and how we apply it to the needs of the Hanneke Lab. Then, I will discuss the circuit board that drives our trap, the vacuum chamber in which our trap lives, and recent upgrades to our system.

2.1 A Motivating Example

To motivate this chapter, consider charges located at the corners of a cube, each with charge +Q. Now, imagine a charge +Q is placed directly at the center of the cube, such that its distance from each charge is the same. While it is tempting to say that the charge is in stable equilibrium from a symmetry standpoint, it is not the case. If a charge directly in the center were to be in stable equilibrium, it must be at a local minimum of potential energy. However, general solutions to Laplace's Equation

$$\Delta\Phi = 0 \tag{2.1}$$

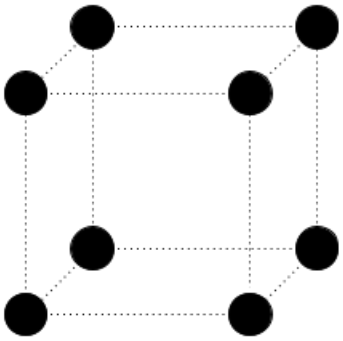

Figure 2.1: Motivating problem to begin thinking about Earnshaw's Theorem. Point charges of all equal charge sit on the corners of a cube. If a point charge is placed at the center, it is not in stable equilibrium. Problem inspired from [19].

tolerate no local minima or maxima. The standard electrostatic potential energy

$$U = Q\Phi$$

cannot provide the function of keeping +Q in stable equilibrium, if Φ is some electrostatic potential. This problem is an example of Earnshaw's Theorem at play, which states that a charged particle cannot be held in stable equilibrium by electrostatic forces alone. Example problem inspired by [19].

2.2 Linear Paul Trap

So, how does one confine a charged particle in three-dimensional empty space? We still require a potential energy minimum in a desired region of space. The trick to circumventing Earnshaw's Theorem is to drop the electrostatic restriction. We can achieve this by using both a static voltage U_0 and a potential of amplitude V oscillating at a radiofrequency. In three-dimensional space, this can be modeled by

$$\Phi = U_0(\alpha x^2 + \zeta y^2 + \gamma z^2) + V\cos(\Omega t)(\alpha' x^2 + \zeta' y^2 + \gamma' z^2), \tag{2.2}$$

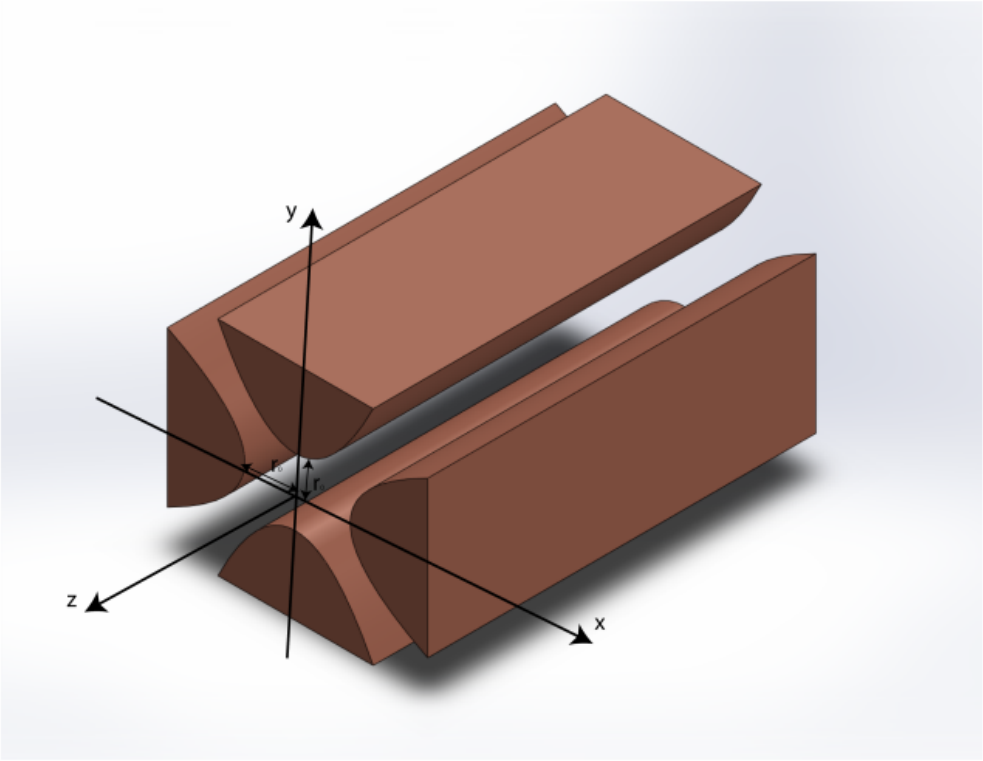

Figure 2.2: Simplified illustration of the Qiao Trap, the Linear Paul Trap used by the Hanneke Lab. Note that in reality two of the electrodes are actually segmented to provide axial confinement.

where Ω is a radiofrequency. The geometric factors, α, ζ , γ, α', ζ' , and γ', paired with Equation 2.1, impose the conditions

$$\alpha + \zeta + \gamma = 0 \tag{2.3}$$

and

$$\alpha' + \zeta' + \gamma' = 0. \tag{2.4}$$

While there are a couple of options for the values of the geometric factors, the linear Paul

trap used by the Hanneke Lab utilizes the following:

$$\begin{aligned} -(\alpha + \zeta) &= \gamma > 0 \\ \alpha' &= -\zeta', \gamma' = 0. \end{aligned} \tag{2.5}$$

The linear Paul trap can be made using four electrodes of near hyperbolical cross-sections that extend along the z-direction, creating a quadrupolar field, as shown in Fig 2.2. The geometric choices given by Equation 2.5 lead to dynamical confinement on the x-axis and y-axis (radially) and static confinement on the z-axis (axially). The linear Paul trap used by the Hanneke Lab was designed by Shenglan Qiao [20] and is known as the Qiao Trap. It uses hyperbolic curvature only at the tips of the electrodes so that we have access to the center of the trap for lasers and imaging.

2.2.1 DC Potential

First, we will take a look at the static portion of the potential. The Qiao Trap applies a DC potential to two opposing electrodes, which are segmented into five sub-electrodes. The outer segments measure 20 mm in axial length, and the three inner electrodes measure 3 mm in axial length to provide axial confinement (as represented in Figure 2.3). The other two electrodes remain solely driven by the RF (to be discussed in Section 2.2.2), though they are capable of independent DC bias if desired.

Other linear Paul traps use endcap electrodes at the axial tips of the trap to provide axial confinement. However, we wish to place mirrors where those endcaps would go so that we can build up laser power for a beam propagating down the trap's axis. This choice leads us to relinquish radial symmetry, so we therefore define our geometric factors as

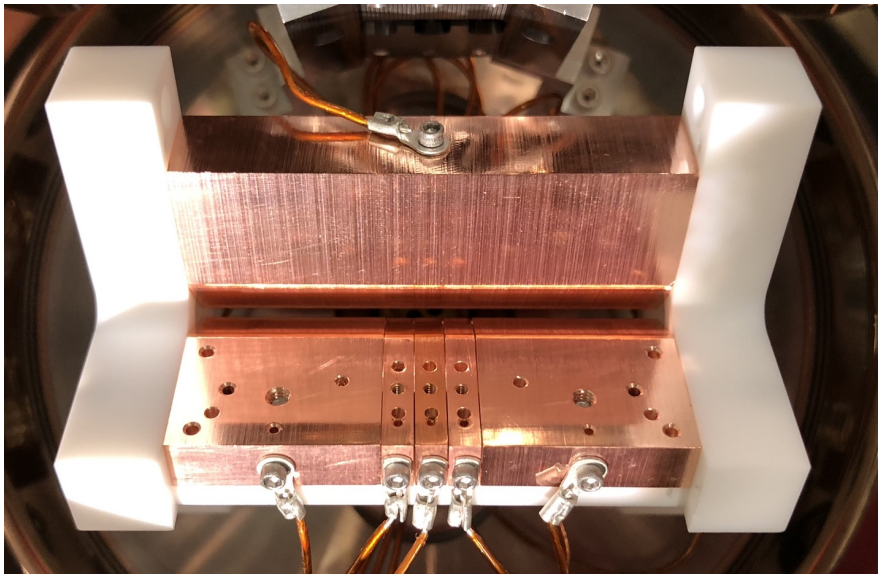

Figure 2.3: Top view from the Qiao Trap. Only two electrodes are in view, with one of them segmented (driven at DC and at an RF) and the other solid (driven at just the RF). For the segmented electrode, the middle three sub-electrodes are 3 mm long each, and the outer two sub-electrodes are 20 mm long each.

$$\begin{aligned} \alpha &= -\frac{\kappa\sigma}{z_0^2} \\ \zeta &= -\frac{\kappa(1-\sigma)}{z_0^2} \\ \gamma &= \frac{\kappa}{z_0^2}, \end{aligned} \tag{2.6}$$

where κ is a dimensionless "fudge" factor due to the electrodes not being perfectly hyperbolic (as well as geometric impurities), z_0 is the axial distance from the center of the trap to the end of the middle electrode (1.5mm), and σ is a constraining parameter to account for the lack of radial symmetry. In a case where we do have radial symmetry, $\sigma = \frac{1}{2}$. The static portion of the field can now be expressed as

$$\Phi_{DC} = \frac{U_0\kappa}{z_0^2}(z^2 - (\sigma x^2 + (1-\sigma)y^2). \tag{2.7}$$

Since the DC electrodes are separated into five subsections, we set them at different voltages U_1, U_2, U_3, U_4, and U_5. In this labeling, U_1 and U_5 are the outer electrode voltages,

U_2 and U_4 are the voltages of the outer 3 mm electrodes, and U_3 is the voltage of the innermost electrode. If U_2 and U_4 are set to the same voltage, we say that U_0 is the difference between U_2 and U_3 [21].

For a singly ionized particle, Equation 2.7 can be represented as done in [22] but with the constraining parameters:

$$\Phi_{DC} = \frac{m}{2|e|}\omega_z^2(z^2 - (\sigma x^2 + (1-\sigma)y^2)) \tag{2.8}$$

where

$$\omega_z = \sqrt{\frac{2\kappa|e|U_0}{mz_0^2}}. \tag{2.9}$$

2.2.2 Dynamic Potential

For the dynamic portion of the potential, all four electrodes are driven with an amplitude of $\frac{V_0}{2}$, where V_0 is the peak-to-peak voltage of the oscillating field. For this quadrupolar field, two opposing electrodes are in phase with one another, while adjacent electrodes are π out of phase with one another.

We define our geometric factors as

$$\begin{aligned} \alpha' &= \frac{1}{r_0^2} \\ \zeta' &= -\frac{1}{r_0^2} \\ \gamma' &= 0. \end{aligned} \tag{2.10}$$

The value r_0 represents the distance from the tip of one of the hyperbolic electrodes to the center of the trap (in a cross-sectional view represented in Figure 2.5). In other words, r_0 is the radial distance from the center of the trap to the tip of the trap electrode, and it is equal to 1.25 mm.

This creates a flopping saddle that oscillates with Ω, as represented Fig 2.4. Each time

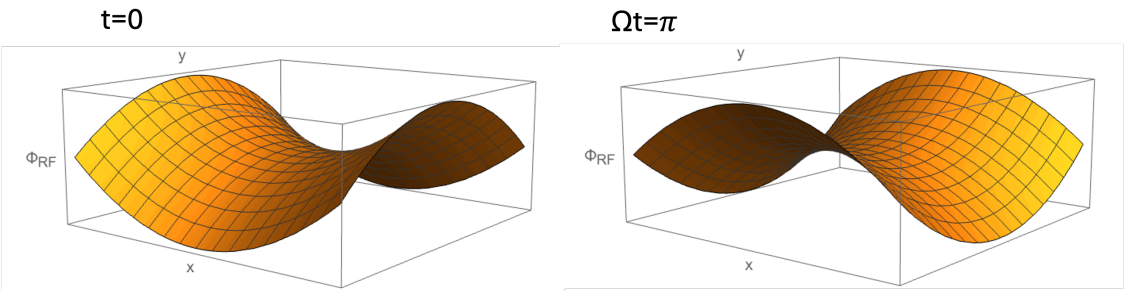

Figure 2.4: A representation of the oscillating potential at t=0 and at a π phase shift later.

the value Ωt increases by π, the potential changes sign, as expected from a cosine function.

For a charged particle found in this potential, the equations of motion are given by

$$\begin{aligned} \ddot{x} &= -\frac{Z|e|}{m}\frac{\partial \Phi}{\partial x} \\ \ddot{y} &= -\frac{Z|e|}{m}\frac{\partial \Phi}{\partial y}, \end{aligned} \tag{2.11}$$

where $Z|e|$ is the charge magnitude and m is the mass of a charged particle. Plugging Equation 2.2 into Equation 2.11, the equations of motion become

$$\begin{aligned} \ddot{x} &= \frac{2Z|e|}{m}[U_0\alpha + V\alpha'\cos(\Omega t)]x \\ \ddot{y} &= \frac{2Z|e|}{m}[U_0\zeta + V\zeta'\cos(\Omega t)]y. \end{aligned} \tag{2.12}$$

With the use of the relations

$$\tau = \frac{\Omega t}{2}, \tag{2.13}$$

$$a_x = \frac{8Z|e|U_0\alpha}{m\Omega^2}, q_x = \frac{2Z|e|V_0\alpha'}{m\Omega^2}, \tag{2.14}$$

$$a_y = \frac{8Z|e|U_0\zeta}{m\Omega^2}, q_y = \frac{2Z|e|V_0\zeta'}{m\Omega^2}, \tag{2.15}$$

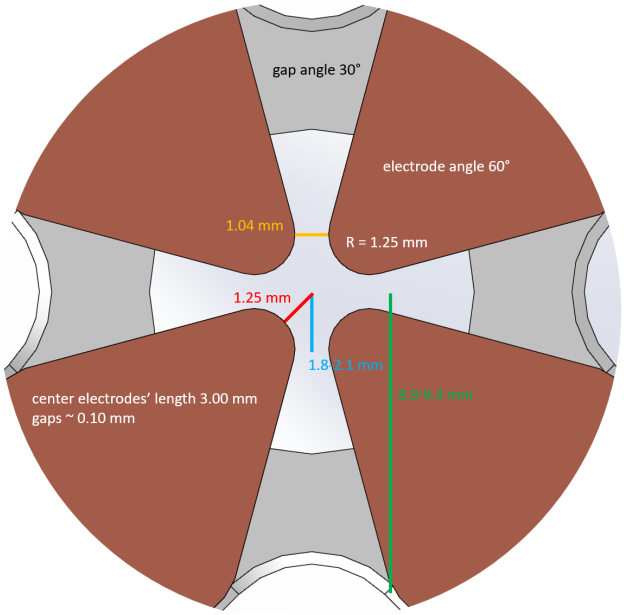

Figure 2.5: Cross section of the trap with the z-axis into and out of the page. Relevant distances are described such as the distance from the tip electrode to the center of the trap, as well as the center electrode length.

the equations of motion (Equation 2.12) can be put in Mathieu differential equation form

$$\begin{aligned} \frac{\partial^2 x}{\partial \tau^2} + [a_x - 2q_x \cos(2\tau)]x = 0 \\ \frac{\partial^2 y}{\partial \tau^2} + [a_y - 2q_y \cos(2\tau)]y = 0. \end{aligned} \tag{2.16}$$

Note that in Equations 2.14 and 2.15, we have placed $\frac{V_0}{2}$ instead of V, where V_0 is the peak-to-peak voltage.

The dimensionless a_i and q_i parameters govern the stability of motion. In stable motion, the amplitude of particle oscillation will not grow over time, but in unstable motion, the amplitude of the particle oscillation will grow over time.

Mathematically, the Mathieu Equations have general solutions with periodic coefficients, C_m's, and a real valued exponent, β_i, where $i \in \{x, y\}$. Following the work of [23–25], the

value β_i^2 in a simplified form can be expressed as

$$\beta_i^2 = a_i - q_i(\frac{1}{A} + \frac{1}{B}), \tag{2.17}$$

where A and B are both continued fraction expressions governed by the C_m coefficients. Regions of stability are bounded by combinations of a_i and q_i that give β_i=0 and β_i=1. However, in the lowest order approximation of ion trajectory, $(|a|, q^2) \ll 1$, it has been determined that

$$\beta_i \approx a_i - \frac{q_i^2}{2}. \tag{2.18}$$

Figure 2.6 represents the lowest region of stability in a plot of q_x versus a_x. Values of V_0, m, r_0, and Ω must be carefully chosen in accordance to the charged particle's properties in order ensure a_x and q_x are in the stable region.

In the case of the Qiao Trap and a singly trapped ion, Equations 2.14 become

$$a_x = \frac{8|e|U_0\kappa\sigma}{m\Omega^2 z_0^2} \tag{2.19}$$

$$q_x = \frac{2|e|V_0}{m\Omega^2 r_0^2} \tag{2.20}$$

Suppose one wants to achieve stability with $q_x = .2$ (equivalent to $q_y = -.2$) for a singly-ionized calcium atom while driving at 10.85 MHz. The electrodes must then be driven at around V_0=300.8 V peak-to-peak.

2.2.3 Pseudopotential Approximation

In the low q limit, where $(|a|, q^2) \ll 1$, a charged particle will experience a harmonic oscillator pseudopotential described in [22] of

$$\Phi_p = \frac{m}{2|e|}\omega_r^2(x^2 + y^2), \tag{2.21}$$

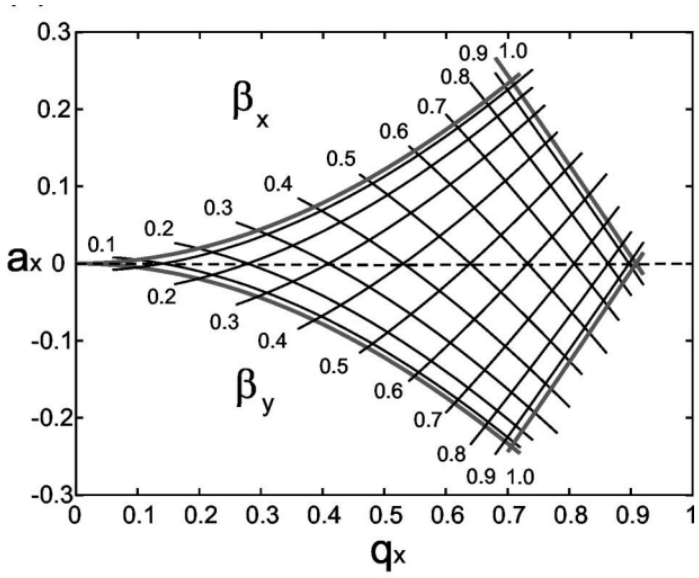

Figure 2.6: Plot of a_x versus q_x in the lowest region of stability diagram for a linear Paul trap. Reprinted with permission from [25] under license number RNP/26/APR/104119.

where the radial oscillation frequency is given by

$$\omega_r = \frac{q_x \Omega}{2\sqrt{2}}. \tag{2.22}$$

However, since our DC potential has radial components, the radial pseudopotential is weakened, and now the total potential in the x and y components can be expressed as

$$\Phi_x = \frac{m}{2|e|}(\omega_r^2 - \sigma\omega_z^2)x^2 \tag{2.23}$$

and

$$\Phi_y = \frac{m}{2|e|}(\omega_r^2 - (1-\sigma)\omega_z^2)y^2. \tag{2.24}$$

This modifies the frequencies in each direction to

$$\omega_x = \sqrt{\omega_r^2 - \sigma\omega_z^2} \tag{2.25}$$

and

$$\omega_y = \sqrt{\omega_r^2 - (1-\sigma)\omega_z^2}. \tag{2.26}$$

Note that we introduce asymmetries to the pseudopotential since our geometric factors in the x and y are scaled by σ and $(1-\sigma)$. To predict the motion of a trapped ion, we must know what our κ and σ factors are, which we simulate in Section 2.2.4.

Note that if q values are very low, which is the regime in which the Qiao Trap operates, there also exists "micromotion" in addition to the "secular" motion described above. This micromotion oscillates at a higher frequency, with smaller amplitudes than the secular motion, and π out of phase with the RF frequency. This occurs the further the particles are from the trap's axis [25].

2.2.4 RF Trap Operating Conditions

We have known that when we run our DC electrodes for axial confinement at U_1, U_2, U_3, U_4, U_5, symmetric choices of U_1 and U_5 do not affect κ, the geometric factor, nor σ, the asymmetric factor introduced by the DC electrodes [21]. Previous work in the Hanneke Lab often set U_3=0. However, sometimes we wish to have deeper potential wells, which can be achieved by letting $U_3 < 0$. Thus, we recalculated κ and σ for different configurations and ratios of U_3/U_2. We used simulation software in order to estimate σ and κ factors.

By simulating their values, we can estimate an ion's oscillation frequency in each direction. We use SIMION software to simulate the potential and fit it to a hyperbolic function in order to find κ, which turned out to remain constant at $\kappa = .17$ for all ratios of U_3/U_2. We then ran fitting functions using the values of κ in order to fit σ to a potential. However, σ showed dependence on the ratio U_3/U_2, as shown by Figure 2.7. As the ratio U_3/U_2 increases, σ increases.

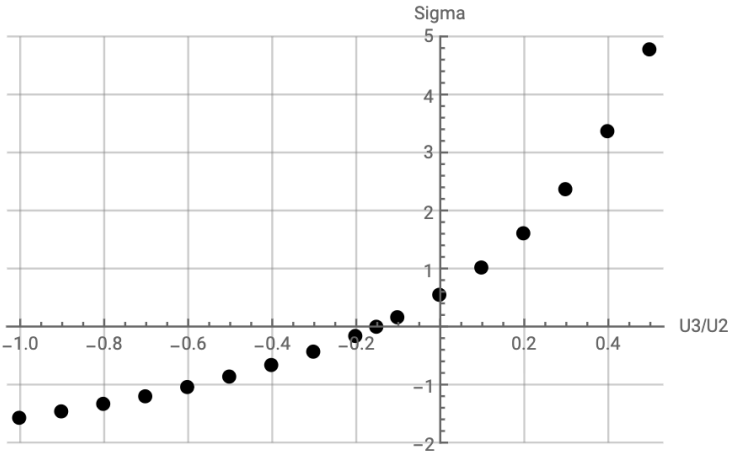

Figure 2.7: σ as a function of the ratio of U_3 –the innermost 3 mm electrode– and U_2 – the outer 3 mm electrodes. As the the ratio increases, so does σ.

2.3 RF Circuit

In order to trap ions in the Qiao Trap, we drive the electrodes with a circuit. This circuit acts as an LC resonator and uses spaces between out of phase electrodes (the adjacent electrodes in Fig 2.5) as the main source of capacitance. In order to achieve small values of q, we must drive the electrodes at voltages around 50-200 V, meaning $\frac{V_0}{2}$ ranges from 50-200V. Typical source generators find these values difficult to drive, so we use a step-up transformer to reach such values. As shown in Figure 2.8, due to the transformer's secondary coil being part of the RF circuit board, it acts as an inductor (which creates the LC resonator). The resonance frequency of this LC resonator should be as high as possible, since high RF frequencies are associated with more tightly bound ions, which need to be close together and near the trap's center in order to be addressed by lasers. The RF frequency of our board ranges between 10.8 MHz and 12.5 MHz [26].

The circuit also introduces the ability to adjust the RF null (the trap's equilibrium position in the saddle of Figure 2.4) by adjusting the relative potential across in-phase electrodes. This is achieved by adding an adjustable capacitor across each electrode, which moves the equilibrium point away from the center of the trap. Having the ability to adjust ion position is helpful in order to ensure that the ions see a uniform beam. Note that this

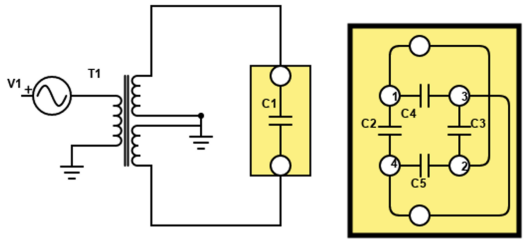

Figure 2.8: A simplified circuit diagram of the LC resonator for the RF drive of electrode potentials. T1 represent the step-up transformer, C1 is the equivalent capacitance of about 20 pF for the electrode-capacitor system, which is shown on the right. Each capacitor between the electrodes is of about 5 pF. Note that this is only one aspect of the full circuit board designed in [26]. Figure credits to [26].

only applies to the 767.6 nm beam that propagates down the trap's axis in an in-vacuum cavity, addressing the oxygen molecules.

Finally, the circuit offers the functions of voltage offset and modulation. The voltage offset allows us to apply static potentials on the segmented electrodes to provide axial confinement and to correct for asymmetries in trap geometry. Finally, the modulation function allows us to test the real frequencies of the secular motion experienced by trapped particles. By driving at a lower frequency than the RF, but in the same ballpark as the expected secular frequencies, we can essentially drive a harmonic oscillator near its resonance frequency. When the trapped particles' amplitudes respond greatly to the modulation, we will know that we are driving at the particles' secular frequencies [26].

2.4 Vacuum Chamber

If there are background gases and particles other than the ones we are trapping, our trapped particles could be knocked out of the potential well. In order to run experiments on trapped particles, they must be able to stay in the trap. Charged particles outside of the trap become useless for the experiment. Thus, we operate our experiments in Ultra High Vacuum (UHV), which is generally defined around 10^{-7} Torr [27], but we ideally want 10^{-10} Torr for our

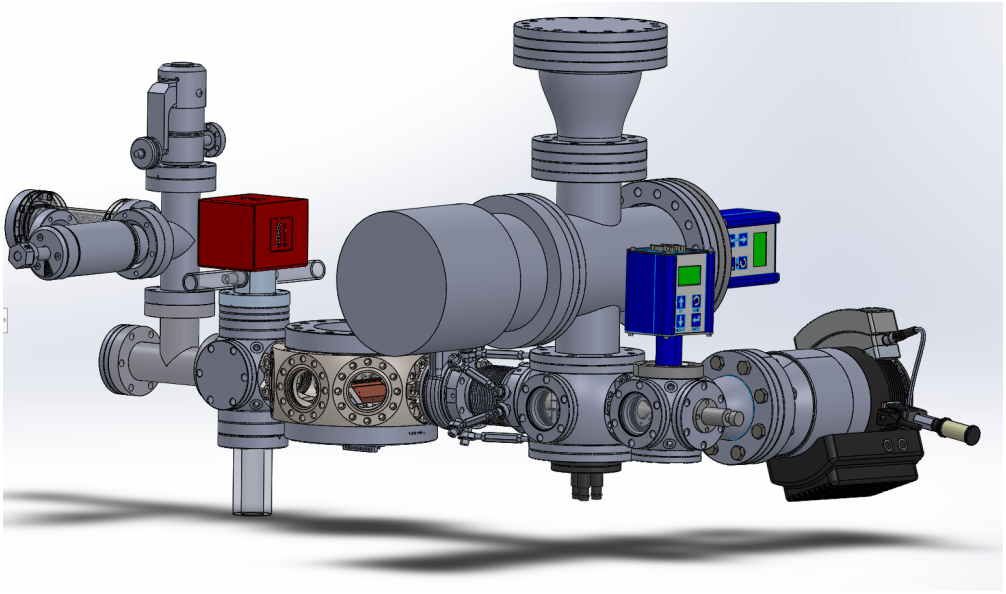

Figure 2.9: SolidWorks model of the vacuum chamber. The length of the full model is about 80 cm in length.

experiments [26]. Important phenomena and components are italicized in this section. The trap chamber used by the Hanneke Lab, as shown in Figure 2.4, is separated into three separate chambers:

1. The Molecular Beam Source Chamber (kept at around 10^{-6} Torr)
2. The Differential Pumping Chamber (kept at around 10^{-8} Torr)
3. The Ion Trap Chamber (ideally kept at around 10^{-10} Torr)

Chambers 1 and 3 both connect to chamber 2 via skimmers, as shown in Figure 2.10. The chamber 1 to chamber 2 skimmer is 1 mm in diameter, and the chamber 2 to chamber 3 skimmer is .5 mm in diameter.

The full trap system is comprised of mostly stainless steel. However, other materials are used, such as:

- Copper for the electrodes, gaskets (used for the connections between chamber parts), and wires.

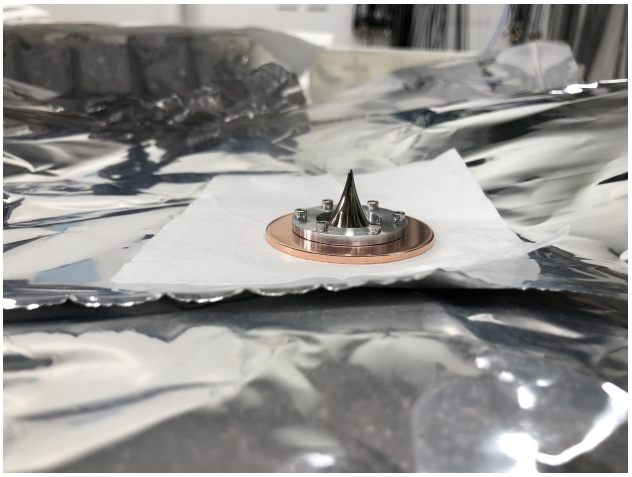

Figure 2.10: Skimmer, used to limit flow between vacuum chambers, on top of a 2.75 inch diameter copper gasket.

- SiO_2 for the six small viewports on the sides of the trap chamber (to send laser beams through) and the larger viewport at the top of the chamber (to allow for imaging of the ions).

- MACOR ceramic comprised of 55% fluorophlogopite mica and 45% borosilicate glass to support the trap [28].

- Plastics (with few outgassing issues) for the electrical connections, insulations, and some valve seals.

When pumping down, it is common to be unable to reach desired vacuum pressures due to a phenomena called *vaporization*. This process begins with intermolecular forces binding solid and liquid molecules to the sides of the chamber. Sometimes, these molecules will vaporize and enter the trap, increasing the pressure [27]. To combat this, we use a process called *"bake-out"*, where we increase the temperature of the trap, ranging from 80°C to 160°C. This process increases the kinetic energy of all desired molecules on the walls of the vacuum chamber. By increasing their kinetic energy, they can transition to gas molecules and then be removed from the trap via the pumps.

Chambers 1 and 2 both use *turbo pumps*, which are cylinders with blades that strike gas

molecules out of the trap chamber [27, 29]. We use the Leybold TurboVac 90i for chamber 1, and we use the Agilent 304 Fs turbo pump for chamber 2. To pump down chamber 3, we use a turbo pump and a diaphragm backing pump. After this, we replace this combination with another combination: a getter pump and an ion pump. This new combination maintains the vacuum pressure. The *ion pump* ionizes gases in the vacuum, attracts them to cathodes, and sends them out of the vacuum. The *getter pump* uses chemisorption, a process in which gases in vacuum bind to the getter surface through chemical reactions. The getter pump's effectiveness in interacting with the gases depends on the cleanliness of the getter surface [27]. When the getter pump is exposed to atmospheric pressure, oxygen and hydrogen films begin to form on the surface, making the pump non-functional. Fortunately, the bake-out process reactivates its effectiveness. We use the NexTorr D 100 pump, which includes both a getter pump and an ion pump [29]. During bake-out, when the bonds between hydrogen or oxygen on the getter surface are broken, they can then be evacuated out of the vacuum via the turbo pump.

In order to monitor the pressure in our vacuum, we use ion gauges in all three chambers. *Ion gauges* operate similarly to ion pumps by first ionizing the gases, then collecting them, measuring the current of collected gases, and converting that current into a pressure reading. We use the Lester 354 Series gauge for chambers 1 and 2, and we use the NR-F-UHV SRS gauge for chamber 3.

During the initial pumpdown, we use a *residual gas analyzer*, the SRS RGA 100, which uses an ion gauge and a quadropole mass filter [30]. We use the residual gas analyzer during intial pumpdown, as it is quite effective at identifying leaks.

2.5 Mechanical Upgrades

Previously, the Hanneke Lab trapped $^{16}O_2^+$ with $^9Be^+$, but new directions have led to the desire of trapping $^{16}O_2^+$ with $^{40}Ca^+$. In order to get beryllium into the trap, we run current

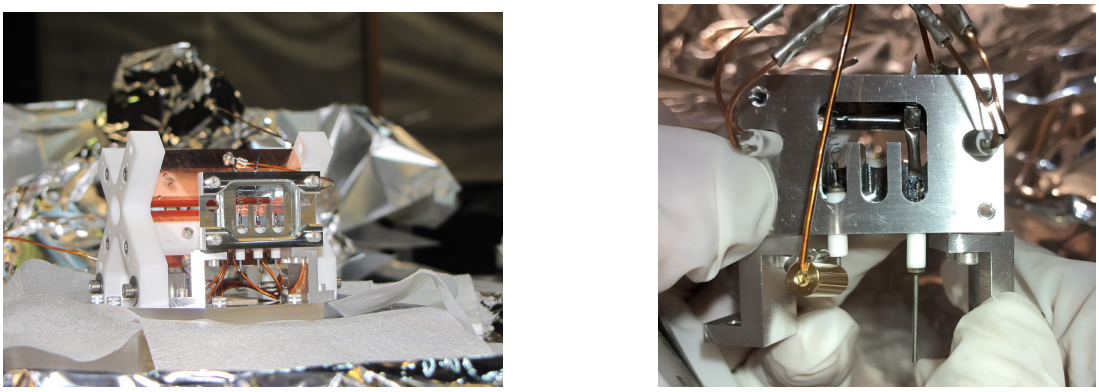

(a) (b)

Figure 2.11: (a) Oven with three beryllium ovens mounted in front of the trap while the trap is out of the chamber (and without the electron guns). Note that this is an old photo. (b) Close up image of the back of the oven mount with one beryllium oven (in the leftmost spot), the newly installed calcium oven (in the rightmost spot), and electron guns wired up. Note that this photograph was taken just before we wired up the calcium oven.

through an oven in a mount (mounted along with other ovens and electron guns). The mount has three spots for ovens, as shown in Figure 2.11. We built an oven to replace one of the existing beryllium ovens, as described Appendix A. The calcium oven is made up of a stainless steel (316) tube with a slit cut in the middle. The top and bottom of the tube are crimped shut, with calcium granules inside of the tube. The ends of the tube are welded to a molybdenum wire and a constantan ribbon for electrical connections.

This upgrading process also involved bringing the trap out of vacuum, opening the trap, installing the oven, rewiring the oven feedthroughs, resealing the vacuum, and pumping back down (see Section A.3). Since the oven feedthrough pins are only rated to 5 A, we could run maximum of 5 A through the oven. However, the calcium ovens needed more current than this, so we used two pins and a 2-1 connection to increase the max current to 10 A. This process required rewiring on both the vacuum side and the air side. After completing these processes, we baked out the chamber for two weeks.

Now, to get calcium into the trap, we run current through the oven assembly, heating it up. This increases the vapor pressure of the calcium, which then escapes through the slit in the stainless steel tube showed in Figure 2.12b.

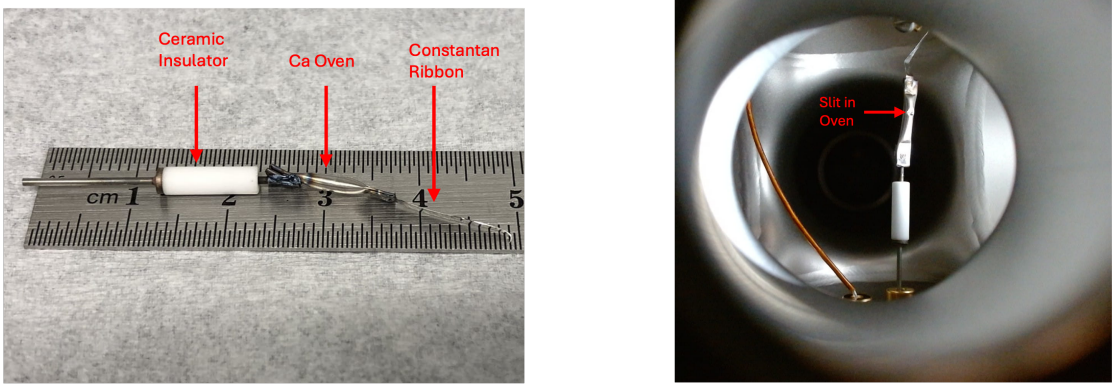

(a) (b)

Figure 2.12: (a) Fully welded oven with labels and a length scale. Note that the slit in the oven where calcium escapes from is not visible. (b) An extra oven in a test chamber for fluorescence testing. Here, the slit is visible.

Chapter 3

Atoms and Optics

The previous chapter discusses the mechanical systems that allow for the trapping of charged particles, and it describes their dynamics inside of a linear Paul trap. However, how does one ionize these atoms such that they can be trapped? How does one prolong an ion's lifetime in the trap? How does one detect that ions are in the trap? This chapter explains the atomic and optical theory that answers these questions and applies it to the needs of the Hanneke Lab.

3.1 Laser Cooling

To get atoms into the trap, we run current through a stainless steel tube or a tungsten wire to heat calcium or beryllium to a vapor pressure that allows gas-phase atoms to enter the trap from an original solid form (granules or wire). This introduces an unfavorable scenario in which the atoms in the trap have too much kinetic energy. If ionized, the atoms will have oscillation amplitudes that are too large to ensure long lifetimes in the trap. Since we address trapped ions using lasers, which can have beam diameters of roughly 1.5 mm, we focus our attention to reducing the ions' oscillation amplitudes. A common technique to achieve this is laser cooling, which also increases the probability that a trapped ion is in its ground state [31]. Specifically, Doppler cooling uses the Doppler shift and spontaneous

emission to decrease an ion's total momentum.

The Doppler shift is a phenomenon that occurs between a source of light and an observer. Generally, this can be expressed as:

$$f_{obs} = f_e(1 - \frac{v}{c}), \tag{3.1}$$

where v is the relative velocity along the line between the observer and the source, c is the speed of light, f_e is the emitted frequency, and f_{obs} is the observed frequency. When the relative velocity is negative, the observer and the source are moving closer together.

An observer moving towards a stationary source will experience a "blue shift" in the perceived frequency, meaning the perceived frequency is higher than the emitted frequency. An observer moving away from the source will perceive a "red-shift" in the perceived frequency, meaning the perceived frequency is lower than the emitted frequency.

Since the charged atoms inside the trap have too much kinetic energy, they will be moving around at higher velocities than desired. If a laser is pointed into the trap and aimed at charged particles, they will observe a Doppler shift in the laser's frequency (assuming the particle's motion is not solely perpendicular to the laser's propagation direction).

Consider the case of alkali-like atoms, where the atom has one valence electron. If a beam is detuned below a resonant frequency for a cycling electric-dipole transition, atoms moving toward the source will observe the beam's frequency as the resonant frequency of the transition. Thus, they will absorb the light and undergo cycling transitions at a much higher rate than those moving away from the source. In the absorption process, the atoms will experience a change in energy equal to hf_0 in magnitude, where f_0 is the resonant frequency of the transition. When the atom's velocity opposes the propagation direction of the light, the absorption event slows the atom down due to a negative charge in the atom's momentum.

In the next step of the cycling transition, the atom transitions from its excited state to a lower state in a process called spontaneous emission. It emits light of the resonant frequency

of the transition [32, 33]. The beauty of this process is that the average change in momentum during emission is zero. This is due to the random direction of emission. Thus, if the atom is moving against the direction of propagation of a laser tuned just below resonance, its atomic velocity will decrease by $\Delta v = -\frac{hf_0}{mc}$ each time it scatters light.

In the general picture, the total change in energy per cycle for the atom can be expressed as

$$\Delta E = -\hbar(\omega_{emitted} - \omega_{absorbed}), \tag{3.2}$$

where $\omega_{emitted}$ and $\omega_{absorbed}$ are angular frequencies of the emitted and absorbed light.

The main goal in the Hanneke Lab is to study the vibrational transitions in $^{16}O_2^+$ in the ion trap. Alkali-like atoms, such as $^9Be^+$ and $^{40}Ca^+$ atoms, are used to sympathetically cool $^{16}O_2^+$ molecules. They serve as the ice cubes for our $^{16}O_2^+$ molecules. Previously, the Hanneke Lab used only $^9Be^+$ as the cooling atom. However, a new coolant atom, $^{40}Ca^+$, provides advantageous properties to the experiment.

In the case of $^{40}Ca^+$, the transition between its $S_{1/2}$ and $P_{1/2}$ states is of wavelength 397 nm, as expressed in Figure 3.1, and it is used as the cooling transition. Additionally, our cooling/detection laser's direction of propagation has projections on all of our trap's axes, so it can cool all three degrees of freedom. Finally, it is also important to note that the spontaneous emission also makes this transition a detecting transition, since we can detect 397 nm light.

3.2 Ion Crystal

When trapped ions are sufficiently cooled through the aforementioned processes, we reach a beautiful result (however, not the final result of the oxygen experiment!). Once cooled sufficiently, a "cloud" of ions inside the trap reaches a phase transition from its disordered, cloud-like state to a discrete, ordered state [34, 35]. This state is referred to as a Coulomb crystal. Coulomb crystals of just Be^+ and a combination of O_2^+ and Be^+ in the Hanneke

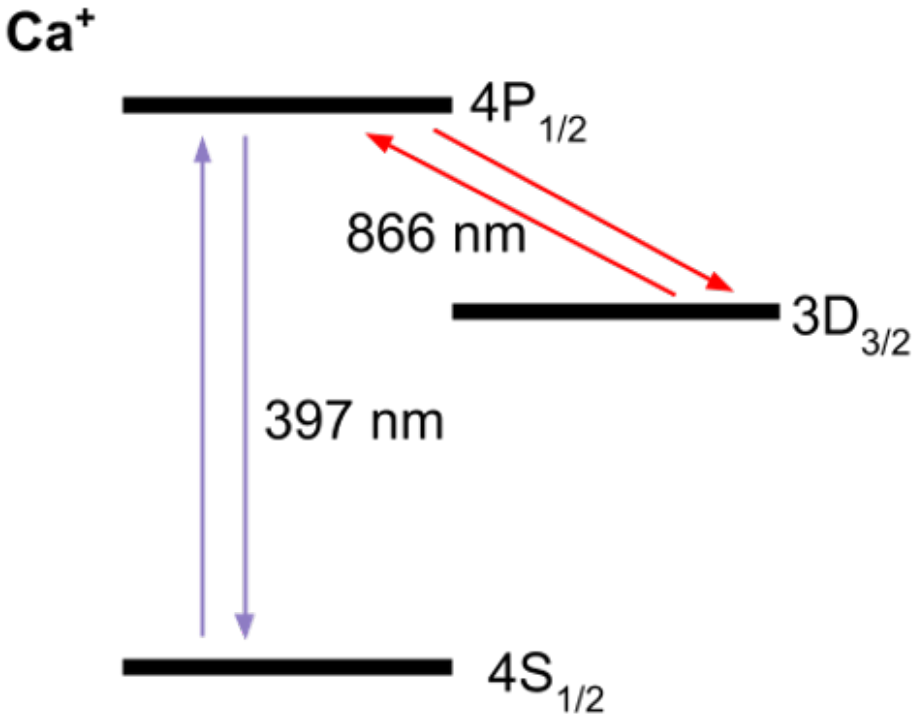

Figure 3.1: Possible transitions with a $^{40}Ca^{+}$ and 397 nm light. A 397 nm laser excites the atom from the $4S_{1/2}$ to the $4P_{1/2}$ state, but the atom can then either return to the $4S_{1/2}$ state or the $3D_{3/2}$ state, where it is unable to move back down to the $4S_{1/2}$ state on its own since it is electric-dipole forbidden. One can use an 866 nm laser to repump an atom stuck in this state back to the $4P_{1/2}$ state.

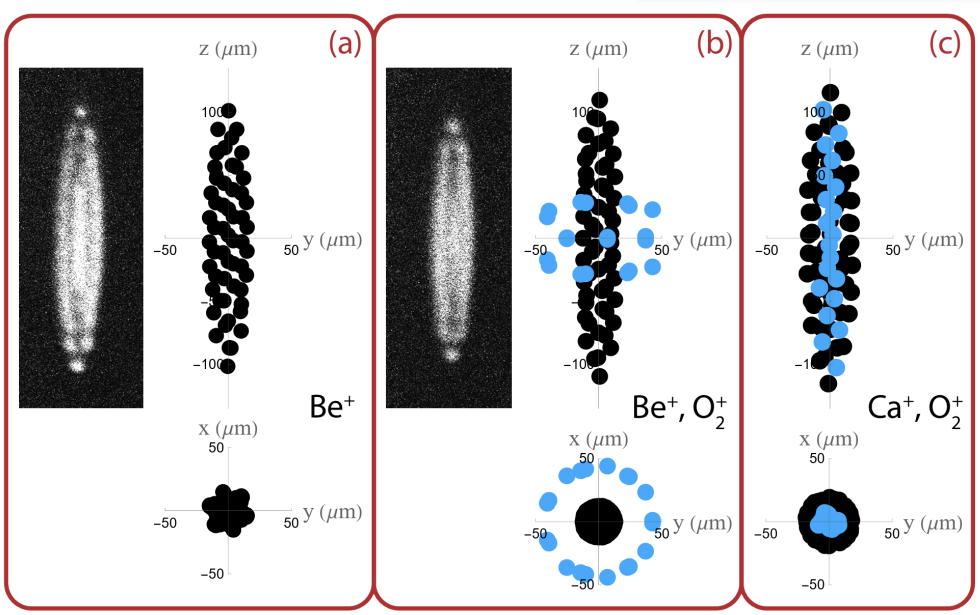

Figure 3.2: Simulations and images of Coulomb crystals of (a) Be^+ atoms on their own, (b) Be^+ atoms (black) and O_2^+ molecules (blue) co-trapped, and (c) simulations of Ca^+ atoms (black) and O_2^+ molecules co-trapped (blue).

Lab have been simulated and imaged (as shown in Figure 3.2).

The radial angular frequency from the pseudopotential (Equation 2.22) has an inverse relationship to the mass of the particle. Thus, a charged particle with a higher mass will be more tightly bound to the trap's axis. This can be seen through the simulations and images in Figure 3.2.

Co-trapping Ca^+ atoms and O_2^+ molecules provides some different and advantageous properties, as compared to the dual-species Be^+ and O_2^+ crystal:

1. Since the Ca^+ atoms will form around the O_2^+ molecules, it will be easier to count how many O_2^+ molecules are in the trap. This is because they appear as a dark core in the center of a fluoresced Ca^+ crystal. The O_2^+ forms around the Be^+ when they are trapped together, making it harder to count the number of O_2^+ molecules in the trap.

2. Since Ca^+ and O_2^+ are more similar in mass than Be^+ and O_2^+, their Coulomb crystals will form closer together. This makes the cooling of O_2^+ more effective by Ca^+ than Be^+. Additionally, there will be more collisions between Ca^+ and O_2^+, which will aid

in the cooling process.

3. The O_2^+ molecules now form a crystal where they are closer to each other. For their vibrational transition, they are addressed by a beam that propagates along the trap's axis. Since they are more tightly bound around the trap's axis, they will see a more uniform beam (see Figure 3.2 for a visual).

4. Following again from their proximity to the trap's axis, the O_2^+ molecules will have less micromotion described in Section 2.2.

5. The lasers needed to drive the transitions in Ca^+ (423 nm, 375 nm, 866 nm, and 397 nm) are much easier to use than the harmonic generations needed for the Be^+ transitions (235 nm and 313 nm).

The cooling transition also serves as a detection transition, since the calcium ion spontaneously emits 397 nm light. This can serve as a way to determine position and shape of the ion crystal. The necessity for the 423 nm, 375 nm, and 866 nm lasers will be discussed in the following sections.

3.3 Photoionization: Ionizing Atoms

In order to trap atoms in the first place, they must be ionized! This can be done in a "dirty" way with an electron gun. This is readily usable in the ion-trap setup, as there are two electron guns mounted in the oven mount, pointing directly towards the center of the trap. However, this can be done in a much "cleaner" fashion through a process called photoionization. This process is defined in [36] as the process where electromagnetic waves are absorbed by a quantum system (Be^+, Ca^+, or O_2^+), making the quantum system eject an electron and therefore ionize. The process of ionizing ^{40}Ca, calcium's most abundant isotope, is two-fold and represented in Figure 3.3.

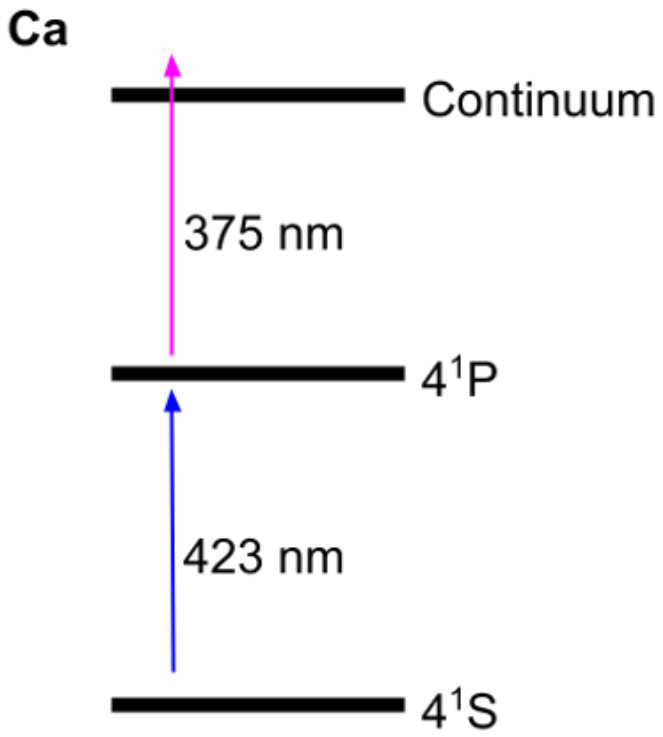

Figure 3.3: Photoionization process of ^{40}Ca through a 423 nm transition and 375 nm transition.

First, neutral ^{40}Ca must be excited from its 4^1S state to its 4^1P state via a resonant 423 nm external cavity diode laser (ECDL). This must be tuned to resonance. A fun trick to test that ^{40}Ca is actually in the trap chamber is to perform the 4^1S to 4^1P transition. If ^{40}Ca is actually present in the trap chamber, it will fluoresce with a wavelength 423 nm. This trick was employed to test a calcium oven's functionality, detailed in Section A.4 and imaged in Figure 3.4.

The next step in this process involves exciting the already excited ^{40}Ca in its 4^1P state with a laser that exceeds the electron's binding energy. This sends the atom into the continuum, where the excited neutral atom becomes an ion plus a free electron. For ^{40}Ca, one can use a 375 nm diode laser to achieve this. This follows from the fact that any laser shorter than 389.8 nm will ionize ^{40}Ca in its 4^1P state (hence, the 375 nm laser does not need to be well tuned)[37]. Now, the particle can be trapped in free space by the Qiao Trap. From

here, the cooling process described in the previous sections can be put to use.

3.4 Repumping

However, there is still a lingering issue in the Doppler-cooling process for trapped calcium ions. By taking a look at Figure 3.1, it becomes apparent that during the spontaneous emission process, $^{40}Ca^{+}$ in the $4P_{1/2}$ state can emit to either $4S_{1/2}$ state or the $3D_{3/2}$ state. This is problematic because Ca^{+} in the $3D_{3/2}$ state cannot find its way back down to the $4S_{1/2}$ state by itself. This arises from selection rules in electric-dipole transitions of $^{40}Ca^{+}$ [9]. Thus, we must repump any $^{40}Ca^{+}$ in its $3D_{3/2}$ state back to its $4P_{1/2}$ state with 866 nm light, where it can either go back down into the $4P_{1/2}$ or $3D_{3/2}$ state. With an ECDL constantly addressing the ions whilst they are Doppler-cooled by the 397 nm ECDL, shelving of $^{40}Ca^{+}$ in its $3D_{3/2}$ state can be prevented, and we can achieve constant Doppler-cooling.

3.5 Optical Systems

To create a scenario in which the linear Paul trap can trap gas-phase $^{40}Ca^{+}$ atoms with $^{16}O_2^{+}$ molecules so that we can image them to study the vibrational transition of O_2, new optical systems are required. These include the optical breadboards for the four transitions (423 nm, 375 nm, 866 nm, and 397 nm) described in Figures 3.1 and 3.3.

The optical breadboards all begin on 12x18-inch or 18x18-inch Thorlabs optical breadboards with External Cavity Diode Lasers (ECDLs) or a diode laser. For the photoionization of $^{40}Ca^{+}$, we use a MOGLabs 423 nm ECDL and a 375 nm diode laser on the same 12x18-inch Thorlabs breadboard. For the laser cooling transition, we use a MOGLabs 397 nm laser on a 12x18-inch board. Finally, for the repumping transition, we use a Toptica ECDL on an 18x18-inch board. Each of these laser-breadboard systems will propagate to some of the following three components before adressing atoms in the trap:

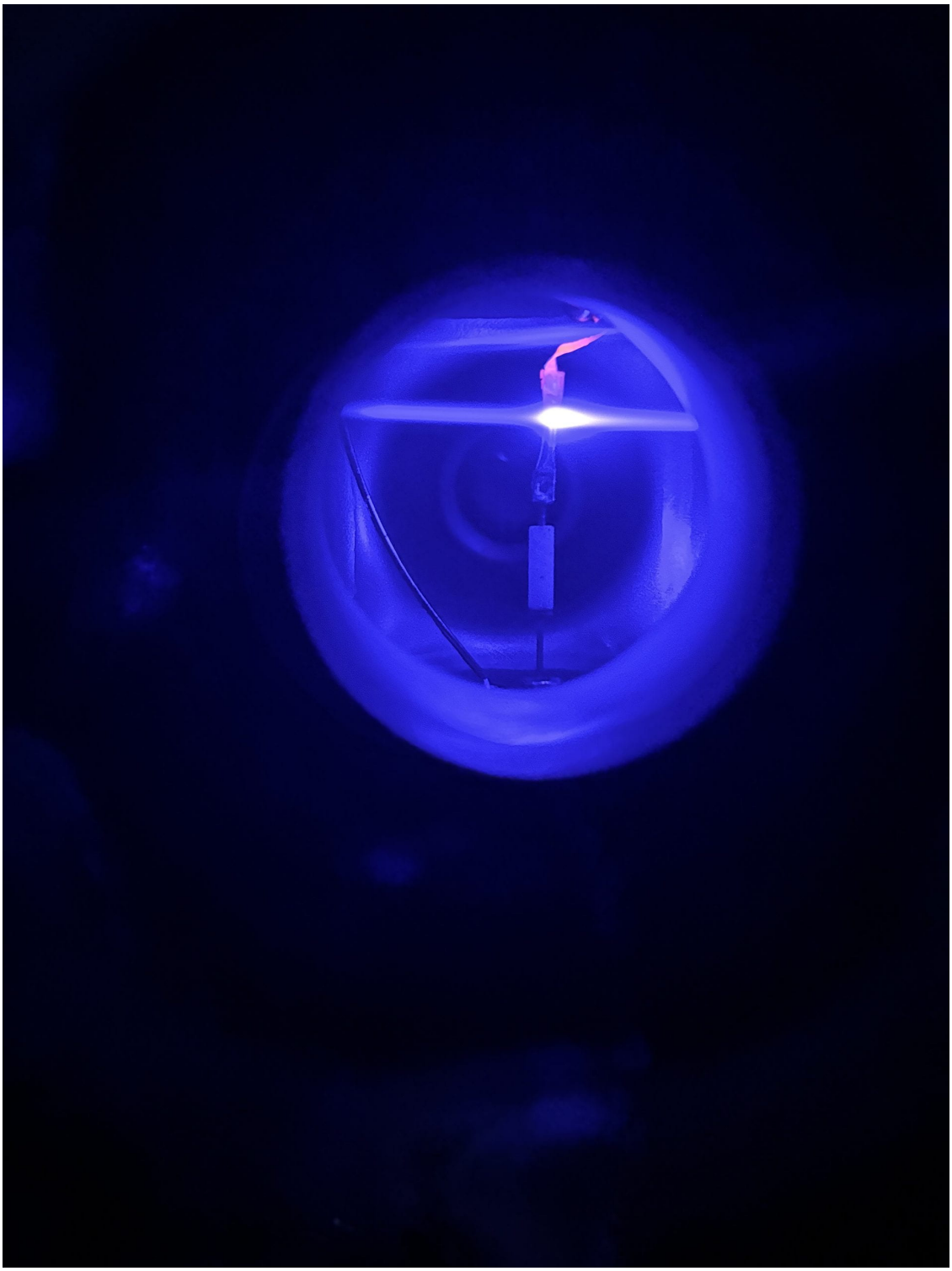

Figure 3.4: Fluorescence of Ca with a resonant 423 nm laser in a test chamber and with an extra Ca oven. We used this to test how much current we would need to run through the oven that was in the real mount and chamber. The oven is connected upright, and the top of the oven (and the ribbon welded for the electrical connection) has a pink thermal glow.

- Wavemeter: This helps us measure the exact wavelength or frequency of the lasers. We use both a Burleigh CW Wavemeter and a Toptica/HighFinesse Wavelength Meter. The Toptica HighFinesse requires much less power for a reading than the Burleigh.

- Fabry-Perot Cavity: This resonator cavity allows us to fight against daily drifts in a laser's frequency due to factors like temperature change. It allows us to lock a laser on its exact desired frequency for desired transitions [38].

- Acousto-Optic Modulators: These allow us to detune lasers at the MHz range. In laser systems that use an AOM, the laser beam is directed to the trap after passing through the AOM. These will be described in better detail in the upcoming discussion.

This section will now discuss the three boards and the important components of each. Important components are italicized in this section.

3.5.1 423 nm and 375 nm Board

The photoionization process, as previously described, involves a bound-to-bound transition (the 423 nm transition) and a bound-to-continuous transition (the 375 nm transition). The laser breadboard is shown in Figure 3.5a.

The Hanneke Lab uses a combination of ECDLs and diode lasers to generate light beams to drive desired transitions. Regular *diode lasers* are semiconductor optical amplifiers that are paired with optical feedback such that if there is sufficient gain, the optical amplifier can be converted into an optical oscillator [39]. This optical oscillator is the laser.

To improve the performance of a diode laser, one can use an external optical resonant cavity to "feed" the laser's light back into itself. These types of lasers are called *external cavity lasers (ECDLs)*. By creating this external cavity for feedback, we can subdue frequency drifts and augment the stability of modes in the laser's output [40]. By adjusting elements of the external cavity, an ECDL can be tuned over a broad range.

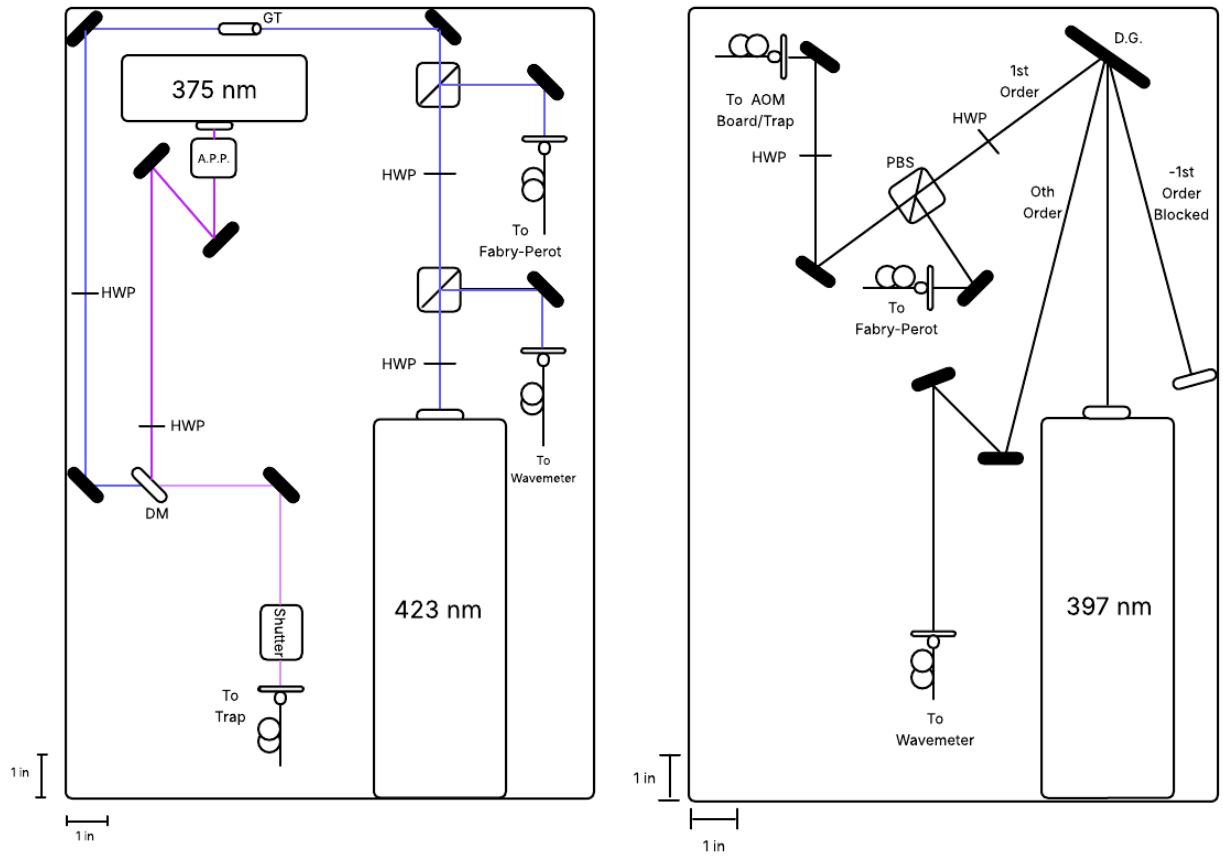

(a) 375 nm / 423 nm Breadboard

(b) 397 nm Breadboard

Figure 3.5: Optical Breadboards for 423 nm, 375 nm, and 397 nm light. A.P.P. is an anamorphic prism pair, D.G. is a diffraction grating, HWP is a half waveplate, QWP is a quarter waveplate, GT is a Galilean telescope, PBS is a polarizing beamsplitter, and DM is a dichroic mirror. We include a shutter in (a) before the coupling to the trap once there are enough ions trapped.

The bound-to-bound transition of ^{40}Ca from the 4^1S to 4^1P state has a natural linewidth of 35.4 $\pm$ 0.3 MHz [37]. Therefore, we will want to tune within this range, and we use an ECDL to achieve this for the 423 nm laser. Since the bound-to-continuous transition only requires a wavelength shorter than 389.8 nm [37], we do not require an external cavity, and we use a laser diode.

Sometimes, beams shapes emerge from lasers elliptically, with waists too large for the desired experiments. When the horizontal diameter is larger than desired, we use an anamorphic prism pair in order to shrink the beam. *Anamorphic prism pairs*, labeled A.P.P. in the

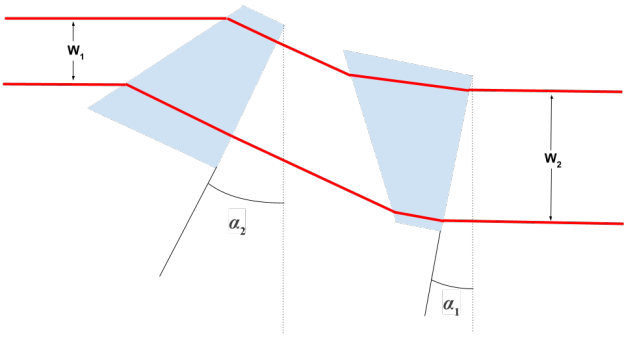

Figure 3.6: Ray diagram detailing how anamorphic prism pairs can alter a beams waist by varying the angle α_1 and α_2. Figure inspired by [42].

laser breadboard diagrams, can change a beam's waist in one dimension and circularize elliptical beams. Anamorphic prism pairs do this by bending light in one direction and keeping the other axis constant. Figure 3.6 shows how the pair works. The second prism should have one of its surfaces at normal incidence and is included to keep the beam propagating in the same initial direction [41]. Different angles of α_1 and α_2 with respect to the vertical axis yield different magnifications according to ThorLabs [42].

The laser breadboard also uses waveplates and polarizing beamsplitters to adjust how much beam power reaches the wavemeters, Fabry-Perot cavities, and the trap. The polarization of an electromagnetic wave refers to the path of its electric field. This electric field is always perpendicular and in phase with its magnetic field. Light can be linearly, circularly, or elliptically polarized. A *waveplate* is a material where the optical axis lies in the plane of the surface itself. As some light (with whatever polarization) propagates through the material, different polarizations change in phase with respect to each other. When this phase shift equals a quarter of the electromagnetic wave's wavelength, we have a *quarter waveplate*. A quarter waveplate also has the property of changing the polarization of an electromagnetic wave from linear to circular, or from circular to linear. When the phase shift through the waveplate is half the wavelength, we have a *half waveplate*. This takes linearly polarized

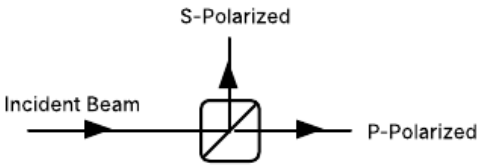

Figure 3.7: In the plane of incidence, when an incident beam hits a cube polarizing beamsplitter, p-polaried light (light polarized parallel to the plane of incidence) is transmitted, and s-polarized light (light polarized perpendicular to the plane of incidence) is reflected.

light and rotates it while preserving its linear polarization [43]. We use half waveplates to control the amount of power passing through and reflecting from polarizing beamsplitters (PBSs).

There are multiple kinds of *polarizing beamsplitters*, but the 423 nm and 375 nm board uses cube beamsplitters. These beamsplitters consist of two different prisms that make a cube once they are glued together by cement (as shown in Figure 3.7). However, there is a dielectric beamsplittter coating at the interface between the prisms [44]. This coating reflects s-polarized light (light polarized perpendicularly to the plane of incidence) and transmits p-polarized light (light polarized parrallel to the plane of incidence). By adjusting half waveplates before the beams reach the PBSs, we can control how much laser power is transmitted or reflected. This way, we can adjust the amount of laser power reaching different parts of our optical breadboards.

As shown in Figure 3.5a, we eventually hope to combine the 375 nm and 423 nm beams and couple them into a single fiber. To combine them, we use a *dichroic mirror* (also known as a dichroic lens) that transmits wavelengths of a certain bandpass and reflects all others. We use Edmund Optics' 400 mm, 12.5 mm Diameter, Dichroic Longpass Filter, which reflects wavelengths of 350nm-375nm and transmits all others [45]. It is labeled in the optical breadboards as DM.

We also use a Galilean telescope for the 423 nm beam, as it must be coupled into a

fiber coupler with an aperture smaller than its beam diameter. In that case, we use -50 mm plano-concave lens and a 100 mm plano-convex lens, to achieve a magnification of .5. A full explanation of how Galilean telescopes work will be given in Section 3.5.3.

3.5.2 397 nm Board

For the cooling of $^{40}Ca^{+}$, we use a MogLabs ECDL, laid out according to 3.5b. An important component to this board is a diffraction grating, labeled DG. *Diffraction gratings* are used in both the 397 nm board, 866 nm board, and all ECDL cavities. They are useful because they diffract different wavelengths of light at different angles. We use reflective gratings, which are created by depositing a ruled, aluminum film onto a glass substrate [43]. These appear as thinly spaced grooves (300 or 1200 grooves per mm, for example).

Reflective gratings diffract different wavelengths of light in differing manners, which is useful for lasers that have broad bandwidths or lasers that may spontaneously emit at the wrong wavelength. If one looks at the optical path of a plane wave hitting a reflection grating in the plane of incidence (according to Figure 3.8), the incident angle and diffracted angles can be related by

$$\sin\theta_d = \sin\theta_i + m\frac{\lambda}{\Lambda}, \tag{3.3}$$

where θ_d is the diffracted angle, θ_i is the incident angle, λ is the wavelength of the plane wave, Λ is the period of the gratings, and m is the order of the different diffracted beams [43].

A 393 nm beam of light could excite an ion in the $4S_{1/2}$ state to the $4P_{3/2}$ state, where it could spontaneously emit to the $3D_{5/2}$ state. This is shown in in Figure 3.9. Since 393 nm is close enough to the desired wavelength for $^{40}Ca^{+}$'s cooling, we care about the bandwidth of our lasers and spontaneous emission. This emphasizes the importance of ECDLs and motivates how reflective gratings become useful. If we propagate our laser beam onto a diffraction grating, we can separate the spontaneously emmited wavelength from the desired

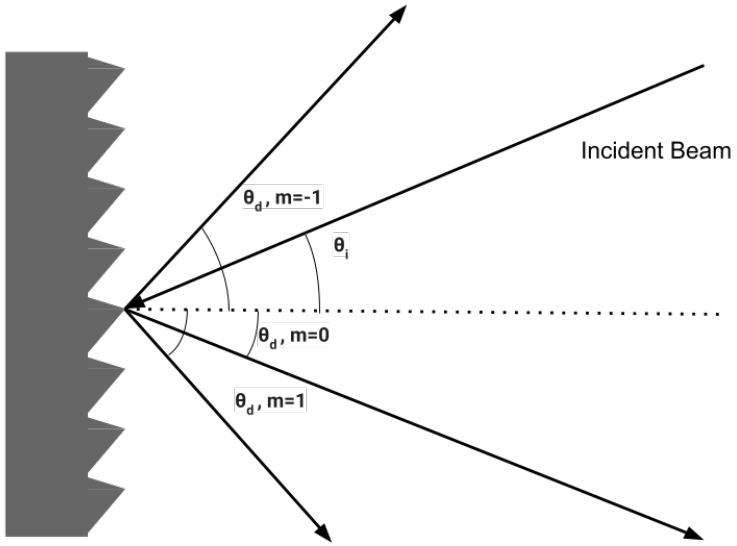

Figure 3.8: Plane of incidence view of a diffraction grating with an m=0 reflected order, an m=1 order, and an m=-1 order.

wavelength.

An additional advantage of using reflective diffraction gratings is that we can also split up different orders of our beams so that they can go to the different necessary functions (wavemeters, stabilization, and AOMs).

For this board, we also use a Glan-Laser polarizing beamsplitter, which consists of two anisotropic crystals with different orientations. Anisotropic material is a medium that has an optical axis where light of any polarization can propagate at the same speed. Ordinary waves and extraordinary waves diffract at different angles within anisotropic material. The term "ordinary waves" refers to waves that are polarized perpendicularly to a material's optical axis, and "extraordinary waves" refers to any light with some component of its polarization along the optical axis [43]. Paired with half waveplates, we can then adjust how much power goes to the stabilization or the trap.

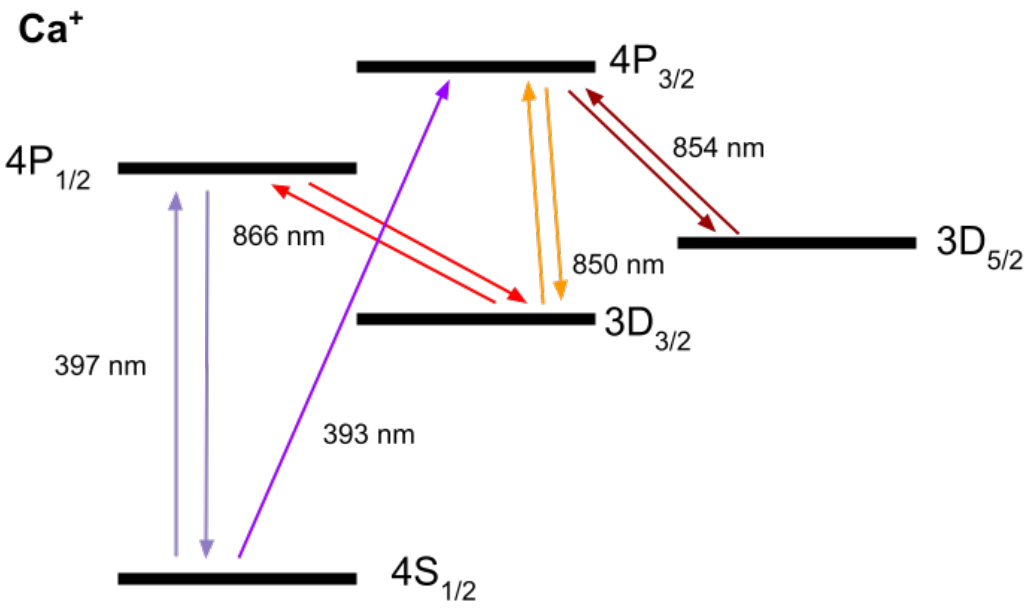

Figure 3.9: A more detailed version of the possible transitions of $^{40}Ca^{+}$. This highlights issues that may arise with a 397 nm or 866 nm laser with broad bandwidths, as they may excite the ion to states where it cannot return to the $4S_{1/2}$ state on its own. This also could occur from spontaneous emission of undesired wavelengths from the laser.

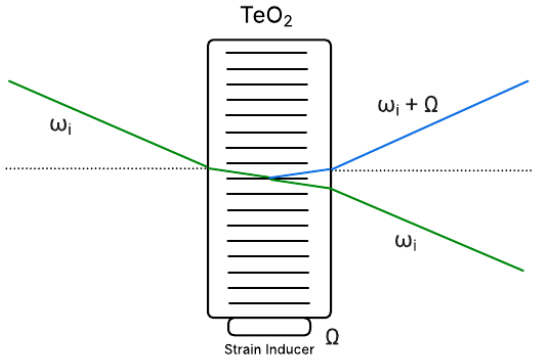

(a) TeO_2 Crystal

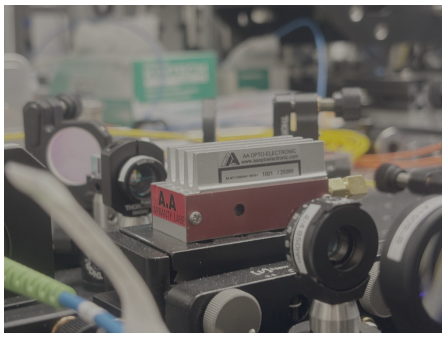

(b) Our AOM for the 866 nm

Figure 3.10: (a) TeO_2 crystal driven at Ω_s diffracting a beam of ω_i. (b) The AA Opto-electoronics AOM used for the 866 nm board. It is mounted on a stage where it can be rotated around finely at different angles, optimizing different orders.

3.5.3 866 nm Board

For the 866 nm repump board, we use a Toptica ECDL, laid out according to Figure 3.11. An important component to this board is the *acousto-optic modulator (AOM)*. AOMs are common tools to achieve frequency modulation. They begin with an AOM crystal that receives an RF signal via a strain transducer. This signal creates an acoustic wave that propagates through the crystal at the speed of sound. This produces an effective diffraction grating with traveling rulings, and diffracted beams appear out the other end of a powered AOM with a new frequency,

$$\omega_d = \omega_i \pm \Omega_s, \tag{3.4}$$

where ω_d is the first diffracted order's frequency, ω_i is the orginal frequency, and Ω_s is the RF signal that the strain inducer is driven at [46]. For the 866 nm beam, we use the AA Opto-electronics MT110-B50A1.50-IR modulator, which uses a TeO_2 crystal. By carefully engineering the beam size and the angle at which the incident beam hits the crystal, we can optimize the power to the first diffraction order, achieving an efficiency of 90.4 ± 3.8 % at an RF of 105 MHz.

An important component of "engineering" an AOM such that it has high efficiency is

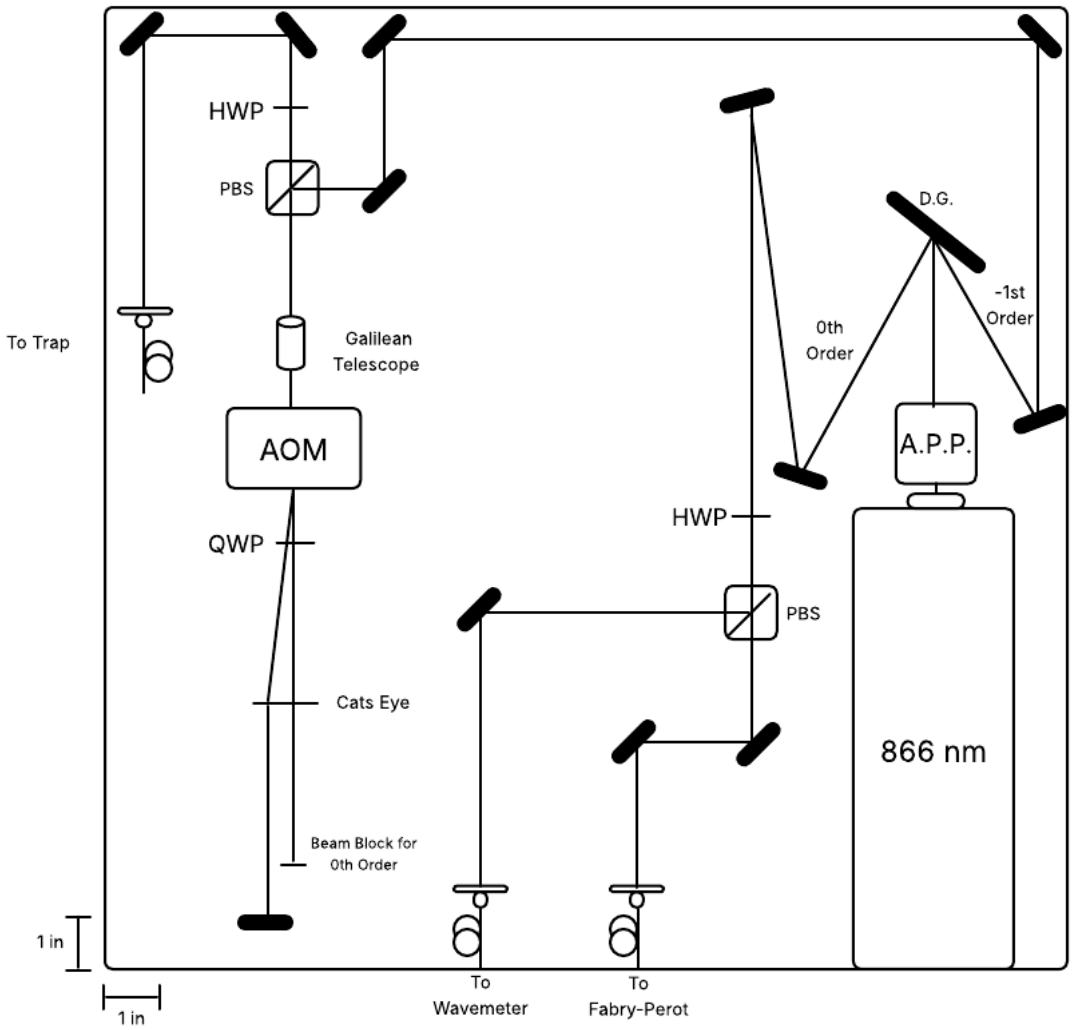

Figure 3.11: 866 nm Toptica ECDL laser breadboard. HWP refers to half waveplates, QWP refers to quarter waveplates, D.G. refers to diffraction grating. Light is split into three paths: to the wavemeter, to the Fabry-Perot Cavity, and towards the AOM (and eventually to trap).

being able to reduce the beam size. The AA Opto-electronics MT110-B50A1.50-IR has an aperture size of 1.5 mm. Beams with diameters larger than this will be clipped at the aperture, reducing the amount of beam power hitting the crystal. This will reduce the AOM's efficiency. However, the active portion of this aperture is often smaller than the aperture itself, which also reduces the AOM's efficiency [46].

A common trick to reduce a beam's size is a *Galilean telescope*. It involves using both a negative focal-length ($-f_1$) lens and a positive focal-length (f_2) lens. If we wish to reduce the beam waist, we have the beam pass through the positive focal-length lens first. However, before the beam comes to a focus, we place the negative focal-length lens at a distance equal to the sum of their focal lengths (remember, one of the focal-lengths is negative). If placed apart at the exact sum of their focal-lengths, the beam will be collimated and reduced by a factor equal to the ratio of their focal-lengths. This can be expressed by

$$\frac{W_1}{W_2} = \frac{f_1}{f_2}, \tag{3.5}$$

where W_1 is the beam's waist after the negative focal-length lens and W_2 is the beam's waist before the positive focal-length lens [47]. To reduce the 866 nm beam before it goes to through the AOM, we use a -15 mm bi-concave lens and a 30 mm plano-convex lens to achieve a magnification of .5. Figure 3.12 highlights how the Galilean telescope works and Figure 3.13 highlights our AOM's enhanced performance after using the Galilean telescope.

As the AOM sweeps, so does the angle of its diffracted order, which poses an issue for fiber coupling (a precise way to transport light). To eliminate this sweeping angle for fiber coupling, we have our beam pass through the AOM twice in what is called a *double pass configuration*. On its second pass through the AOM, it is modulated once again and propagates antiparallel to its original propagation through the first pass. This means the beam's modulation is twice that of a single-pass beam.

This configuration can be achieved (as shown in Figure 3.11) by placing a quarter wave-

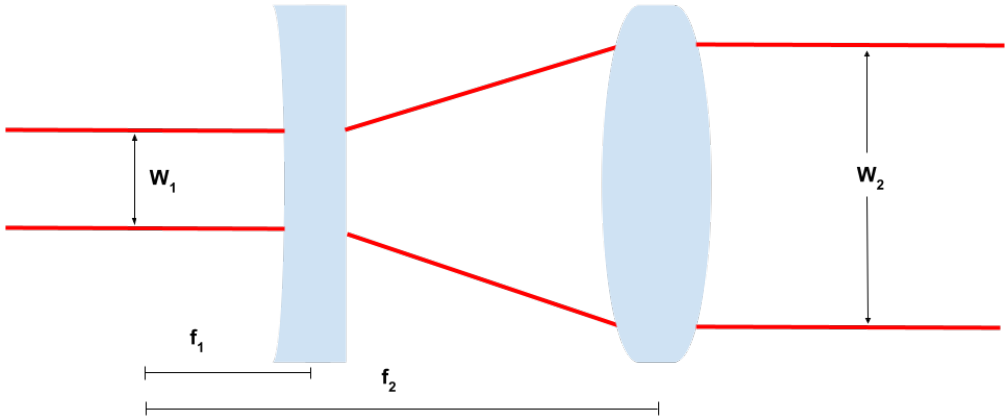

Figure 3.12: Beam magnification or expansion via a Galilean telescope, which uses a positive focal-length lens (the plano-convex lens on the right) and a negative focal-length lens (the plano concave lens on the left). Depending on the direction of propagation, an incident beam will be reduced or expanded in diameter.

Figure 3.13: The AA Opto-electronics MT110-B50A1.50-IR AOM's first order efficiency with (in red) and without (in blue) the Galilean telescope of magnification .5. When using the Galilean telescope, we get better efficiency at every driving frequency.

plate after the AOM, followed by the plano-convex lens (which serves as the cats-eye retroreflector) with a focal length equal to the distance from the AOM crystal to the lens. On the other side of the lens, a focal-length distance away, is a mirror that reflects the beam back through the lens, the quarter waveplate, the AOM, and the Galilean telescope. A beam block is placed between the cats-eye and the mirror to block the zeroth-order beam.

The *cats-eye retroreflector* allows us to frequency tune without concern of misaligning the beam through the AOM on the second pass (or anywhere along the beam path after the first pass through the AOM). This follows from the fact that the diffracted angle from the crystal changes as the modulation frequency changes. As the frequency modulation is swept, light rays propagate from the center of the lens and emerge from the other end, parallel to the beam's zeroth diffracted order, with a spatial separation. This spatial separation is a function of the frequency modulation (and hence the RF), but since it is always parallel to the zeroth order, we can adjust the mirror so that the rays are always normal to it and aligned back through the AOM. This is only possible if the lens is placed exactly at its focal-length away from the AOM crystal. This way, the alignment through the AOM in both passes is invariant with respect to the applied RF. Without a cats-eye retroreflector, the double pass would only be aligned for a tiny range of modulation [46].

Figure 3.11 can also help illustrate the importance of the quarter waveplate. After the second pass, it will have essentially worked as a half waveplate, rotating the polarization of the beam by $\frac{\pi}{2}$. We initially get the beam to propagate towards the AOM via a cube polarizing beamsplitter (and by fine-tuning it with two adjustable mirrors beforehand). Thus, on its second pass, it will be transmitted through the polarizing beamsplitter and can then be fiber coupled.

Additionally, when we run a 100 mA injection current through the 866nm Toptica ECDL, it has a vertical diameter of 0.576 $\pm$ 0.003 mm and a horizontal diameter of 1.89 $\pm$ 0.02 mm. To achieve the desired magnification for this beam, we oriented anamorphic prisms at $\alpha_1 = 31^\circ$ and $\alpha_2 = 0^\circ$ to obtain a magnification of 3.4 $\pm$0.1. Since the prisms were

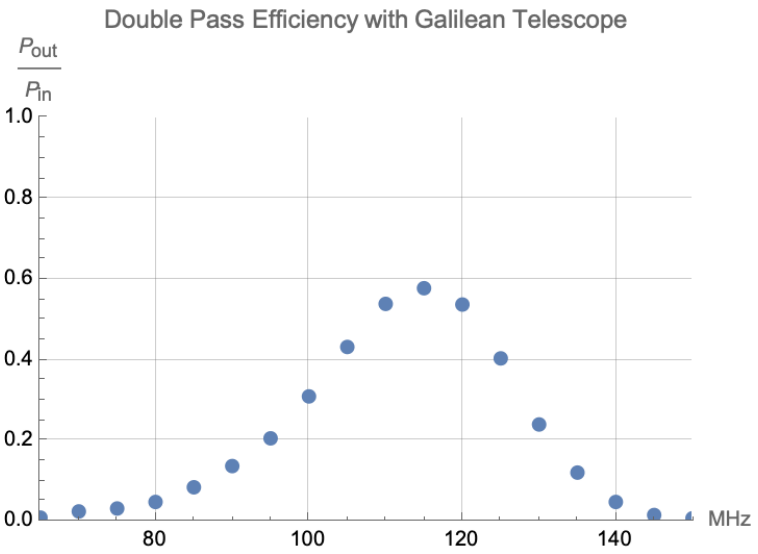

Figure 3.14: The AA Opto-electronics MT110-B50A1.50-IR AOM's first order efficiency through the double pass configuration.

unmounted, we machined a mount, as detailed in Appendix B.

3.5.4 Fiber Optics

To transport beams from their original optical breadboards to the trap, the wavemeters, and the stabilization, we use fiber-optic coupling and cables. *Fiber optics* involve optical fibers and fiber couplers. *Optical fibers* are used to transmit light over long distances. They consist of an inner core made of silica glass (of index of refraction n_1) where light propagates, and an outer cladding with a higher index of refraction (n_2) than the core [43]. For the light that goes to the wavemeters and stabilization boards, we use single-mode fibers that do not maintain polarization. *Single-mode fibers* have small inner core diameters such that only one transverse mode is allowed to propagate through the fiber [48].

At the trap, we care about the polarization of our light, so we transport that light through polarization-maintaining fibers, which are single-mode fibers that maintain linearly polarized light. We place a half waveplate before coupling to the polarization-maintaining fibers to align the beam polarization with the fast or slow axes of the fiber.

Light can only be guided through a fiber from air under certain conditions. To direct the

beam into the core, we use *fiber couplers*, which consist of small focal-length lenses, to bring the beam to focus at the point where it meets the core. For single mode fibers, a beam of light should be on the fiber's axis with a Gaussian beam distribution, and the beam's waist should should match the mode field diameter of the fiber [49]. If they are matched, we can achieve desirable coupling efficiencies.

We use ThorLabs fixed focal-length couplers, adjustable focal-length couplers (which can have their focal lengths adjusted via a screw), and FiberPorts (which have five degrees of freedom and a rotation adjustment), depending on our needs. For example, we want to couple both the 375 nm and 423 nm beams into a single fiber as it goes to the trap. Since we are trying to couple two beams of different wavelengths (sufficiently far apart), they will require an achromatic lens, which brings light of different wavelengths to the same focal point. The FiberPort from ThorLabs is the only coupler with such a lens, so we use it for the 375 nm and 423 nm inputs towards the trap.

The angle at which the beam hits the fiber core also governs how well the light is coupled into the fiber. While a beam may be directed to hit the small core, it may be at an angle such that the beam is not lined up with the fiber's axis. Thus, it is necessary to "walk" the beam into the fiber to adjust the angle at which the beam hits the core. This can be done if there are four degrees of freedom, which can come from two adjustable mirrors or one adjustable mirror and a coupler on a kinematic mount. At the output (Figure 3.15), when we want the beam to propagate through the air again, we use fiber couplers to collimate the beam.

3.5.5 Towards the Trap

The beams coupled into the polarization-maintaining fibers are output near the trap, where they pass through a viewport and propagate towards the center of the trap. To combine all beams onto one path, we use two different dichroic mirrors. We use walking techniques to ensure each beam passes through the center of the trap on the same path. We also use an

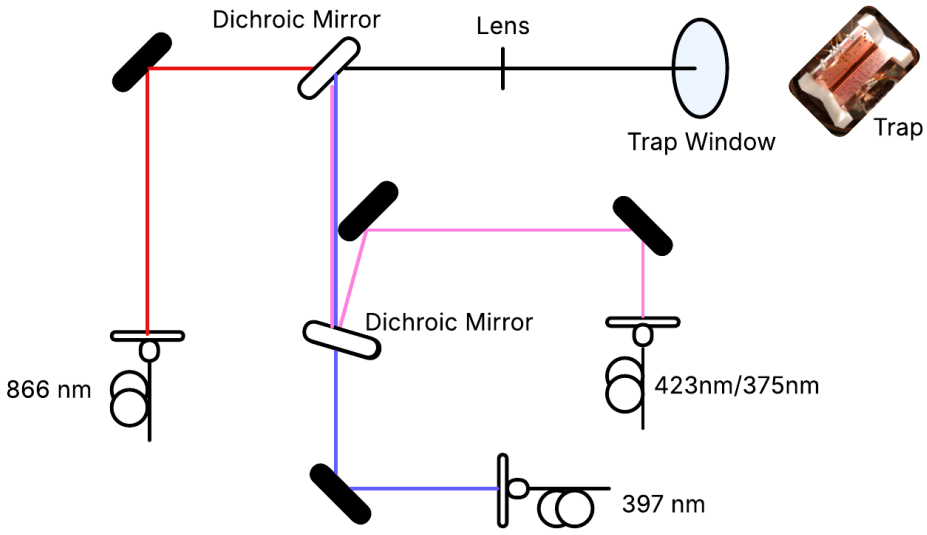

Figure 3.15: All three laser breadboards couple into polarization-maintaining fibers and are output by the trap, where they are all combined and sent along the same beam path, 45° with respect to the trap's axis. Note that this is not to scale.

achromatic lens that focuses the light at the center of the trap (where we expect ions to be). Figure 3.15 shows the optical paths of the outputs before they enter the trap. Note that we send the beams at an angle of 45° with respect to the trap axis (and the x-y plane is rotated 45° as well), so our beams' propagation directions have projections on all three of the trap's axes.

3.6 Imaging the Ions

Once we have $^{40}Ca^{+}$ in the trap with the beams aimed and focused directly at them, we can image the ions. Note that we rotate the trap's x-y plane by 45° so that we can place the imager directly above the trap's top view port, with a view to the center of the trap (in between electrodes). We view the ions via an imager that is able to detect the spontaneously emitted 397 nm light. We use the Thorlabs FBH400-10 bandpass filter to ensure that we do not image light of the other laser frequencies. We can monitor ions by magnifying them (in an image) through a lens and a camera. This lens has three degrees of freedom: along

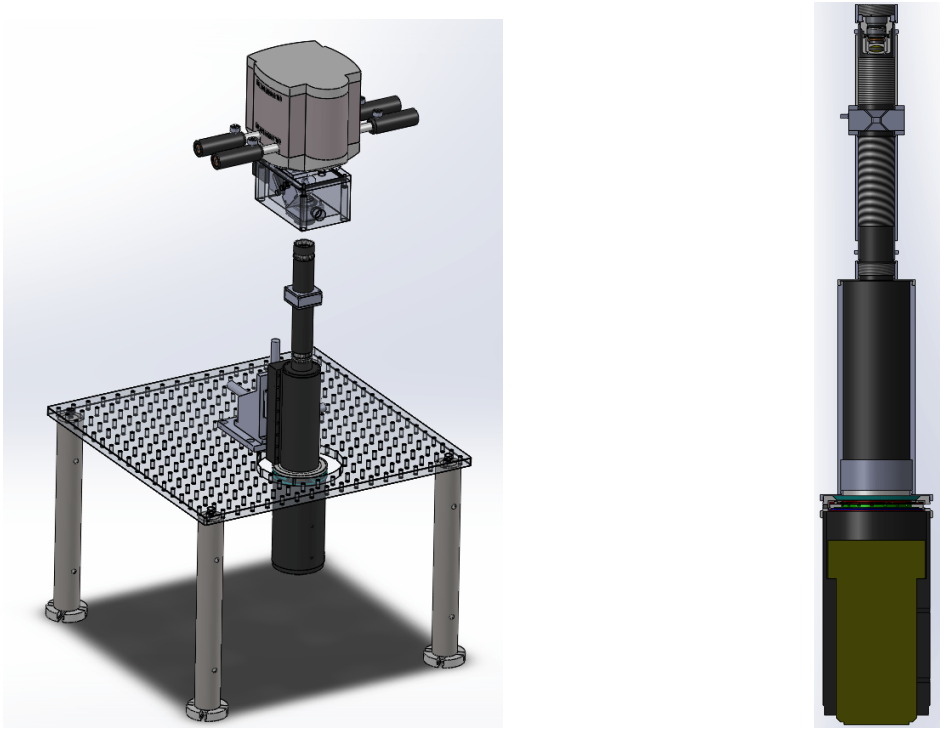

(a) Full Imager Set-Up (b) Lens Tube

Figure 3.16: SolidWorks models of our imager, which sits suspended atop a table so that the bottom of the imager tube sits above the top-view port of our trap chamber. Note that the suspended table in (a) is an 18x18 inch board, and (b) is about 60 cm long.

the trap's axis, across the trap (in between the gaps in the electrodes), and an up-down axis (which adjusts the focus). We use an Andor iXon3 885 camera, as represented in Figure 3.16, operated by Micro-Manager Software. To calibrate our field of view, one can measure the distance using the across and along degrees of freedom between two known positions (two corners of a segmented electrode, for example). From here, the field of view can be calculated.

Chapter 4

Results

With the ultimate goal of measuring the vibrational transition of $^{16}O_2^+$ with a new cooling atom, we needed to design, construct, and put together new mechanical and optical systems for $^{40}Ca^+$. This used much of the same theory and equipment as $^9Be^+$, but it required us to make two major upgrades to the ion-trapping system:

- Build and install an oven to get calcium into the trap
- Design and construct a four-laser system to drive the transitions of ^{40}Ca

In this chapter, I will show how we successfully ionized and trapped $^{40}Ca^+$; drove the cooling, detection, and repumping transitions; and imaged different ion configurations. However, I will begin by briefly discussing the simulations of ion crystal formations.

4.1 Ion Position Simulations

With values of σ and κ for different DC wells simulated in Section 2.2.4, we can solve for the a and q parameters from Equations 2.14 and 2.15. From there, we can find the charged particle's ($^{40}Ca^+$) oscillation frequencies in each direction for different amplitudes of the RF potential. Then, in Wolfram Mathematica, we can minimize the energy of a system of N

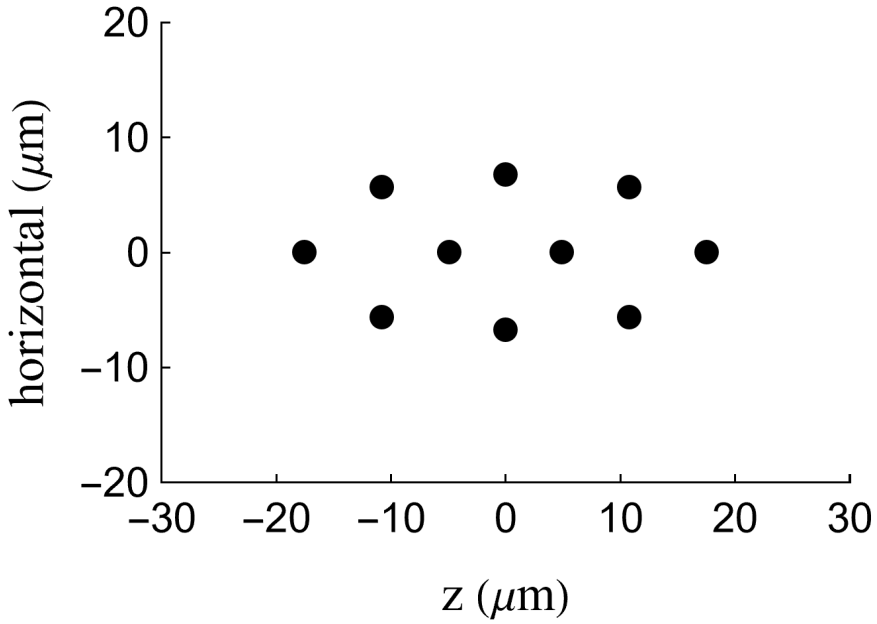

Figure 4.1: Simulated ion-crystal shape in the view of the imager for 10 ions in an RF field of 10.85 MHz with an amplitude of 280 V peak-to-peak and a DC well configuration of $(U_1, U_2, U_3, U_4, U_5) = (10, 10, -5, 10, 10)$ V. The axis titled "horizontal" highlights that this is the projection onto our field of view.

ions oscillating at the determined frequencies and experiencing the Coulomb force. We can then plot their expected ion crystal formation.

We plot the expected ion crystals in the plane in which we view them through the imager. In our trap/imaging system, the trap has its x and y axes in Figure 2.2 rotated 45°. This is done so that our imager (which is facing downwards) can image in between the gaps of the electrodes. Figures 4.1, 4.2, and 4.3 show the ion crystal simulations for different N amount of ions, RF voltages, and DC wells.

Note that these images are projections onto our horizontal plane of view. Additionally, from these simulations, it becomes clear how adjusting the DC well and the RF peak-to-peak voltage can affect a crystal's shape. A deeper DC well means the ions will be more tightly confined axially, limiting their ability to extend across the trap's axis. Figure 4.3 has the shallowest well (governed by U_2, U_4, and U_3) of -6V, but it has the highest RF peak-to-peak voltage of 325 V. Thus, the ions are more likely to extend along the z-axis and less likely to position themselves away from the RF null. Thus, they form a line extending on the

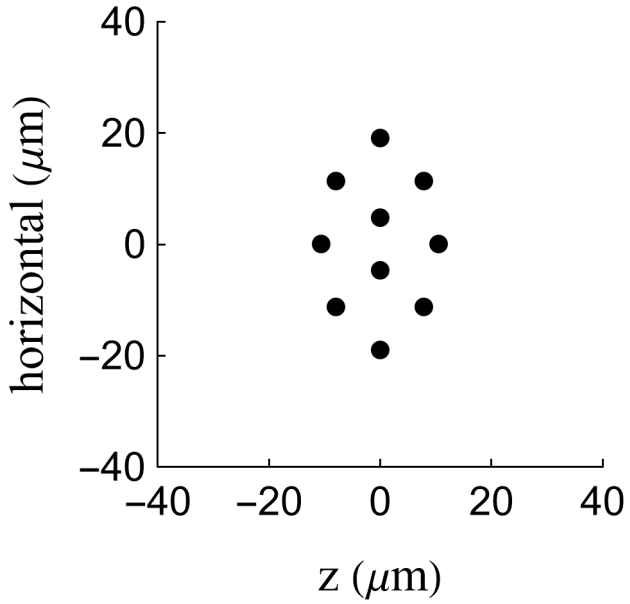

Figure 4.2: Simulated ion crystal shape in the view of the imager for 10 ions in an RF field of 10.85 MHz with an amplitude of 252 V peak-to-peak and a DC well configuration of $(U_1, U_2, U_3, U_4, U_5) = (10, 10, -8, 10, 10)$ V. The axis titled "horizontal" highlights that this is the projection onto our field of view.

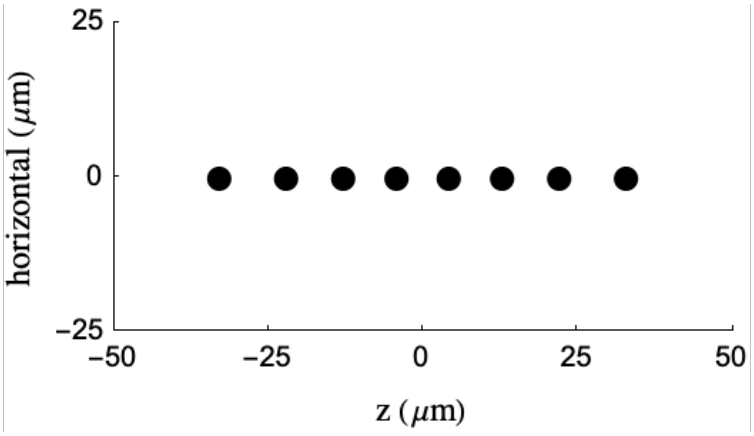

Figure 4.3: Simulated ion crystal shape in the view of the imager for 7 ions in an RF field of 10.85 MHz with an amplitude of 325 V peak-to-peak and a DC well configuration of $(U_1, U_2, U_3, U_4, U_5) = (10, 6, 0, 6, 10)$ V. The axis titled "horizontal" highlights that this is the projection onto our field of view.

z-axis. Figure 4.1 shows how deepening the potential well and decreasing the RF voltage can cause the ions to "buckle" and take positions away from the RF null due to more axial confinement and less radial confinement. In this case, the DC well is -15 V deep and the RF peak-to-peak voltage is 280 V. Figure 4.2 shows that as we continue to deepen the DC well (in this case to -18 V) and decrease the RF peak-to-peak voltage (to 252 V), we can increase the degeneracy in axial position and have ions further away from the RF null.

4.2 Trapping Ions

Physically, we trap ions using the theory and methods described in Chapters 2 and 3. First, with the AOM for the 866 nm board tuned to 110 MHz modulation and with our lasers fiber coupled to the wavemeters, we began tuning our lasers. ECDLs can be fine tuned by adjusting a piezo voltage applied to a piezo-electric transducer, which allows us to move an optical element in the external cavity [50]. However, we needed to adjust the MogLabs ECDLs more broadly to reach our desired wavelengths. One can achieve this by adjusting the position of the grating inside of the external cavity via a screw.

Using these techniques and according to the NIST Atomic Spectra Database's expected frequencies [51], we tuned our lasers to 755,222.46 ± .06 GHz for the 397 nm laser, 709,078.24 ± .06 GHz for the 423 nm laser, and 345,999.85 ± .07 GHz for the 866 nm laser. Resonance is actually 346,000.07 GHz for the $3D_{3/2}$ to $4P_{1/2}$ transition, but since we use a double-pass AOM, which adds .22 GHz to the frequency, we tuned our laser .22 GHz below. In the end, we found the best efficiency for ion crystal loading while running the 397 nm laser at 755,222.20 ± .06 GHz, the 423 nm laser at the resonance frequency of 709,078.23 ± .06 GHz, and the 866 nm laser at 346,000.18 ± .07 GHz. It makes sense for the 397 nm laser to be tuned below resonance, due to the blue-shift effect experienced by the atoms in the Doppler cooling process.

On the trap side, we made sure the lasers were propagating and focused at the center of

the trap using walking techniques and a 150 mm focal length lens (positioned 150 mm away from the center of the trap, as shown in Figure 3.15). The output powers at the trap side were 7.2 ± 0.2 mW for the 397 nm beam, 6.5 ± 0.2 mW for the 423 nm beam, 1.4 ± 0.1 mW for the 375 nm beam, and 13.0 ± 0.4 mW for the 866 nm beam. These powers were not set for any particular reason, and we expect that we could successfully load and cool $^{40}Ca^{+}$ at lower powers.

Next, we began loading calcium ions by running 7.00 ± 0.02A through the calcium oven. However, as we continued to dump (a process described below) and reload ions, we could run the oven at 6.00 ± 0.02 A. Once we began to see ion crystals form, we would turn off the oven and block the 423/375 nm beam in order to stop the loading of ions in the trap.

Figure 4.4 shows a singular trapped ion. We were able to calculate the view of the imager using techniques describes in Section 3.6, but this time we used the ions and the vertical edges of the field of view as references. We found the images to have a 230 ± 5 μm horizontal field of view for 1004 pixels (which is how size reference bars are calculated). From here, we cropped all of the images of the ions from the full image. It is important to note that the ion size in the image is not the actual size of the atom. It appears much larger here due to a mix of optics resolution and ion motion, and the same applies for all imaged ions to be presented in this chapter.

When we ran the oven with the photoionization beam unblocked for longer periods of time, we trapped more ions. When we want to dump ions out of the trap and start a fresh load, we set our DC well to $(U_1, U_2, U_3, U_4, U_5) = (10, 5, 0, -5, -10)$ V, effectively creating a slide for ions so they can leave the trap. Alternatively, we can turn the RF off, which will also dump particles out of the trap. Figures 4.5, 4.6, and 4.7 show multiple-ion configurations, as well as the configurations overlaid with their simulated positions. They all correspond to the same RF frequency of 10.85 MHz, but with different peak-to-peak voltages and DC wells.

Figure 4.5 corresponds to the trap parameters used in Figure 4.1: 280 V peak-to-peak

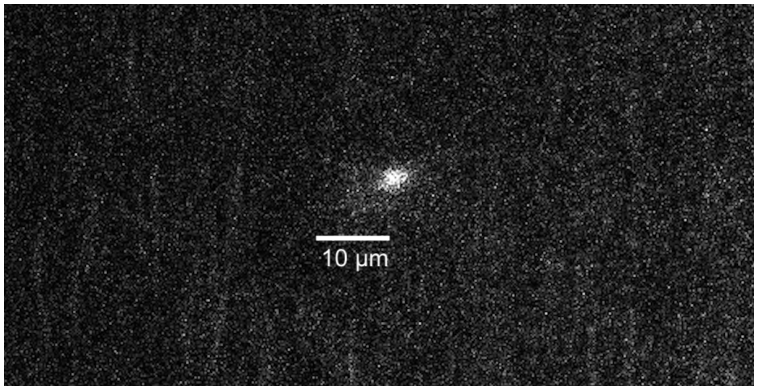

Figure 4.4: Single trapped $^{40}Ca^{+}$ ion inside of the Qiao Trap. We ran the RF field at 10.85 MHz with an amplitude of 278 V peak-to-peak and a DC well configuration of $(U_1, U_2, U_3, U_4, U_5) = (10, 10, -5, 10, 10)$ V. Note that the ion size in the image is not the actual size of the atom, but it appears much larger here due to a mix of optics resolution and ion motion.

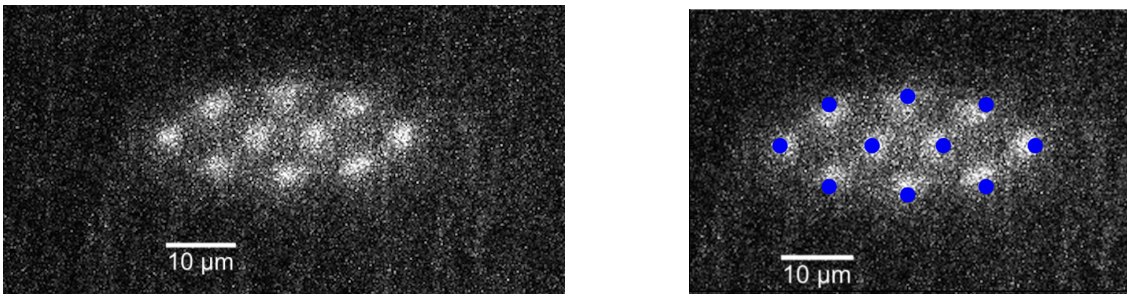

(a) (b)

Figure 4.5: (a) 10-ion crystal with an RF frequency of 10.85 MHz, 280 V peak-to-peak voltage, and a DC well configuration of $(U_1, U_2, U_3, U_4, U_5) = (10, 10, -5, 10, 10)$ V. (b) The real 10-ion crystal overlaid with its simulation. In both, the trap's axis is along the left/right direction and the "horizontal" (which references our field of view, consult Section 4.1) corresponds to the up/down direction.

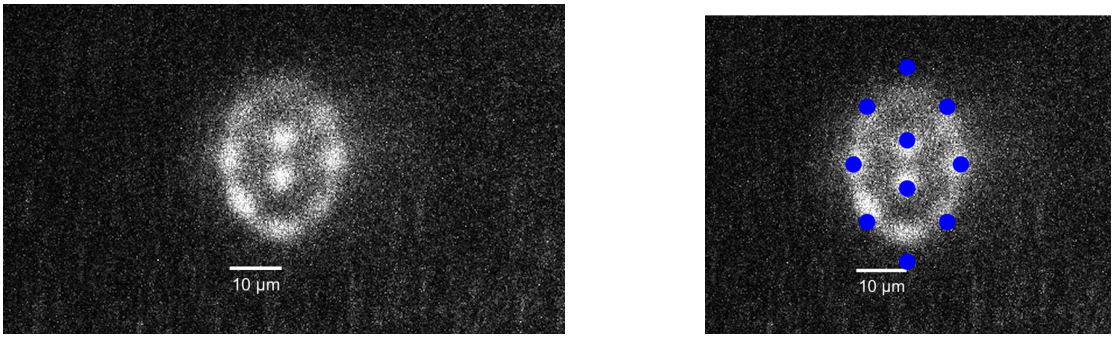

(a) (b)

Figure 4.6: (a) A 10-ion crystal with an RF frequency of 10.85 MHz, 252 V peak-to-peak voltage, and a DC well configuration of $(U_1, U_2, U_3, U_4, U_5) = (10, 10, -8, 10, 10)$ V (b) The real 10-ion crystal overlaid with its simulation. In both, the trap's axis is along the left/right direction and the "horizontal" (which references our field of view, consult Section 4.1) corresponds to the up/down direction.

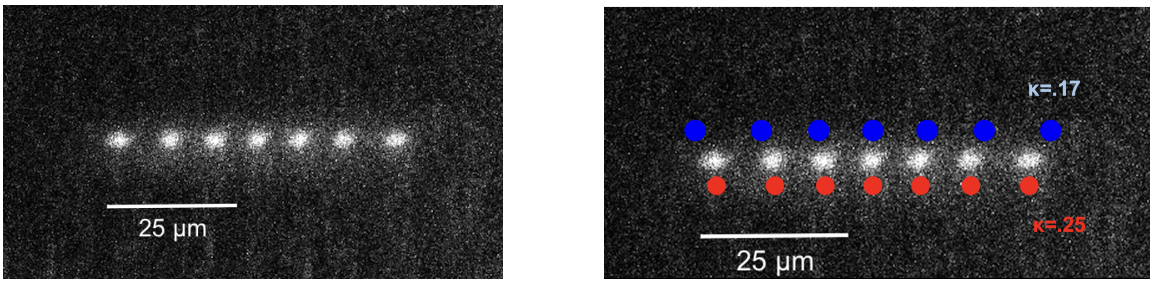

(a) (b)

Figure 4.7: (a) A 7-ion crystal with an RF frequency of 10.85 MHz, 325 V peak-to-peak voltage, and a DC well configuration of $(U_1, U_2, U_3, U_4, U_5) = (10, 4, 0, 4, 10)$ V (b) The real 7-ion crystal overlaid with simulations of different values of κ and a DC well of -4 V. In both, the trap's axis is along the left/right direction and the "horizontal" (which references our field of view, consult Section 4.1) corresponds to the up/down direction.

voltage and a DC well of -15 V. Figure 4.6 corresponds to the trap parameters used in Figure 4.2: 252 V peak-to-peak voltage and a DC well of -18 V. Figure 4.7 corresponds to the trap parameters used in Figure 4.3 apart from a small tweak in the DC well: 325 V peak-to-peak voltage and a DC well of -4 V.

When we apply a deeper DC well and a lower RF peak-to-peak voltage, the ion crystal configures itself with more axial degeneracy and is able to have ions further away from the trap's axis. Axial degeneracy means multiple ions have the same position along the trap's axis (same value of z in our defined coordinate system). This is due to tighter axial confinement and looser radial confinement. As we increase the RF peak-to-peak voltage and make the DC well shallower, the ions begin to configure themselves with less axial degeneracy and closer to the trap's axis. This stems from decreased axial confinement and increased radial confinement. Finally, as we continue making the DC well shallower and the RF peak-to-peak voltage higher, the ions show no axial degeneracy and take positions all along the axis (with no visible radial deviation).

While all imaged ion crystals agree with the shape of their simulated ion crystal, there are some small discrepancies. In Figure 4.6, the location of the top and bottom ions do not fully agree with the simulations, and the ions are not well focused in the image. The simulations calculated their positions to be further away from the center of the crystal than they appear in the real image. However, according to the simulated formation in Figure 4.2, they should both be around 20 μm away from where our horizontal plane is zero, which is the focal plane for our imager. This means that the ions could be about 20 μm away from the focal plane, so they would be out of focus in the image. This could explain the discrepancies in their overlaid plot in Figure 4.6b. See Figure 4.8 for a visualization of this focal plane.

Figure 4.7 shows another discrepancy. The simulated ion crystal (using κ =.17) plotted in blue, does not perfectly overlap with the the real image of the seven-ion crystal. However, we could get them to line up by increasing κ in the simulations to .25, plotted in red. This discrepancy could be due to the differences between the simulated electrodes and the as-built

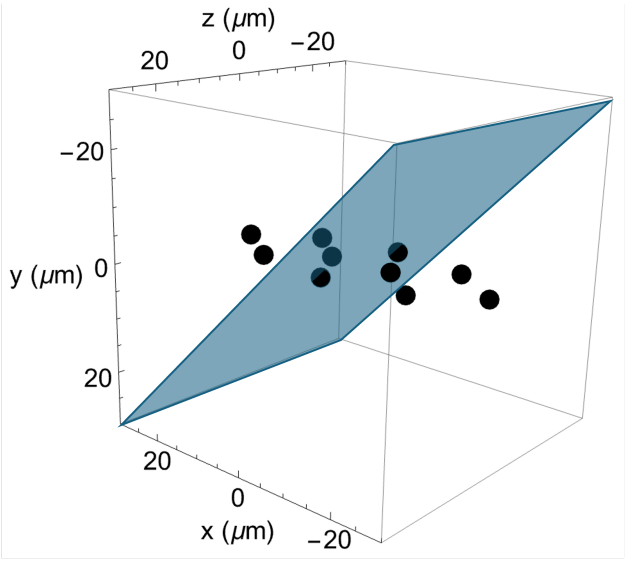

Figure 4.8: The focal plane, graphed in light blue, with the simulated crystal corresponding to the -18 V potential well and 252 peak-to-peak voltage. This illustrates how the ions furthest from the focal plane will not be in focus.

electrodes, which could cause κ to change as a function of the DC well.

It should also be noted that while trapping these crystals, the ion gauge was reporting the pressure of the chamber to be hovering around 3×10^{-8} Torr to 1.5 $\times 10^{-9}$ Torr. This is a higher pressure than we would like, as we ideally want the ion trap chamber at around 10^{-10} Torr. Being able to get the chamber pressure back down to 10^{-10} Torr would give us better resolution on these images and increase the lifetime of the ions in the trap. For example, our ions' lifetime in the trap did not last past a lunch break that was under an hour long, but certain ions have been demonstrated to have lifetimes ranging up to multiple days [52].

4.3 Interesting Configurations

During the trapping process, we also found some other fascinating ion configurations. Figure 4.9 shows two different ion configurations. Figure 4.9a has an RF frequency of 10.85 MHz, 240 V peak-to-peak voltage, and a DC well configuration of $(U_1, U_2, U_3, U_4, U_5) = (10, 10, -6, 10, 10)$ V. Figure 4.9b has an RF frequency of 10.85 MHz, 288 V peak-to-peak voltage, and a DC well configuration of $(U_1, U_2, U_3, U_4, U_5) = (10, 10, -6, 10, 10)$ V. These

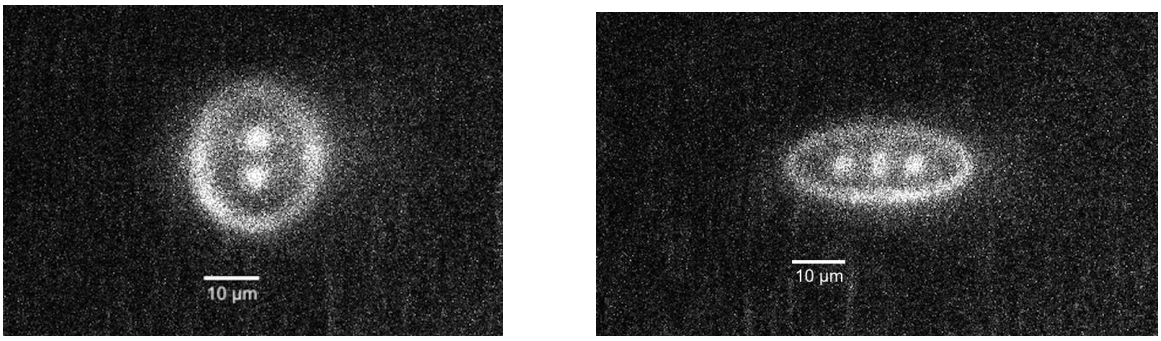

(a) (b)

Figure 4.9: (a) Melted state ion crystal with an RF frequency of 10.85 MHz, 240 V peak-to-peak voltage, and a DC well configuration of $(U_1, U_2, U_3, U_4, U_5) = (10, 10, -6, 10, 10)$ V. (b) Melted state ion crystal with an RF frequency of 10.85 MHz, 288 V peak-to-peak voltage, and a DC well configuration of $(U_1, U_2, U_3, U_4, U_5) = (10, 10, -6, 10, 10)$ V.

formations consist of a discrete set of ions on the inside of a fluorescing ring, which takes elliptical shapes.

The shift from discrete ion formations to continuous ring-like formations is considered a melting transition. This melting transition occurs after a Coulomb crystal (which is formed at low temperatures [22]) experiences a temperature increase, which leads to thermal fluctuations, and ions experience diffusive motion [53]. During this process, the ions start to move with increasing speeds in elliptical or circular paths, which get imaged as continuous rings. Some theories explaining the melting transition have been studied by other ion-trapping groups [53, 54]. One theory is that the melting transition depends on the amount of ions in the trap and trap anisotropy. Trap anisotropy refers to a trapping potential having differing properties along different axes. The further ions move from the trap's axis, the more susceptible they are to the micromotion described in Section 2.2.3. Thus, the Doppler shift and cooling rate will be position dependent, which could explain why the continuous ring forms around discretely trapped ions that are very close to or on the axis [54].

Chapter 5

Conclusion

Taking a step back and looking at the bigger picture, the Hanneke Lab is on the hunt for new physics. In the end, we hope test for drifts μ, the proton-to-electron mass ratio, over time. Probing this ratio over time will allow us to search for new physics and test for dark matter, which has demonstrated the potential to cause drifts in fundamental constants [12, 55]. To do so, we will use the vibrational transitions from the $v = 0$ state to the $v = 16$ state of $^{16}O_2^+$ as a probe for these drifts. The vibrational degrees of freedom for molecules are related to the motion of the inertial masses of the nuclei, while the chemical bonds relate to the mass of the electron. Thus, drifts in vibrational frequencies of $^{16}O_2^+$ will point towards drifts in μ.

In order to achieve this, we trap $^{16}O_2^+$ in a linear Paul trap, along with atoms to sympathetically cool the trapped-ion system. The Hanneke lab has previously been able to co-trap $^{16}O_2^+$ and $^9Be^+$. However, $^{40}Ca^+$ was determined to possibly be a better candidate for co-trapping, due to its larger mass. Over the course of the past year, we went from an already working ion-trap system for $^{16}O_2^+$ and $^9Be^+$, and we successfully built and designed the optical and mechanical systems in order to trap $^{40}Ca^+$ with $^{16}O_2^+$. This work involved constructing and installing a calcium oven, as well as designing, laying out, and constructing a four-laser system in order to drive the photoionization and cooling process. However, the four-laser system still has much room for improvement, and future projects can build

towards measuring the vibrational frequency of $^{16}O_2^+$.

5.1 Future Additions to the Laser System

5.1.1 Laser Stabilization

All three laser breadboards for the transitions of ^{40}Ca have a laser beam that can be coupled to Fabry-Perot cavities. In the future, we will want the lasers to remain at the same frequency for as long as they run. When dealing with atomic transitions, which have narrow linewidths, it is not ideal to have lasers wandering in frequency. Thus, we will want to use these cavities in order to correct from daily drifts in laser frequency [38]. Getting these cavities up and running is a crucial next step.

5.1.2 AOM for the 397 nm beam

Our current set up for the 397 nm board (Figure 3.5b) has a polarization maintaining fiber coupled towards the trap. However, in the future, this will be coupled to a separate AOM board, before it is coupled again to the trap. The board has the ability to go to the trap with or without AOM, which is why we were able to image $^{40}Ca^+$. Adding this AOM will allow us to modulate the frequency for the laser cooling transition, which is very important to the overall cooling of the experiment. Additionally, it will allow us to have a fast shutter, as we can prevent alignment of the beam into fiber couplers by either turning the AOM off or adjusting the frequency modulation in a single-pass configuration. The lab currently has an AOM board for a 313 nm laser beam, which was used for the cooling/detection transition from the $^2S_{1/2}$ to $^2P_{3/2}$ states in $^9Be^+$. The set-up uses the Intra Action Corp ASM-802B8, which is anti-reflection coated for 300-400 nm and modulates at a central frequency of 80 MHz. A concern is that the efficiency of the AOM is proportional to the RF power but inversely proportional to λ^2. Since we are using the AOM with a larger wavelength, we will need more RF power. A next step would be to see if this set-up works for the 397 nm beam.

This will allow us to either have a working AOM set-up for the 397 nm beam, or guide us to figure out what equipment to buy for a new AOM board.

5.1.3 Shutters

When we successfully loaded ion crystals in Section 4.2, we used a manually placed beam block in front of the 375/423 nm beam going to the trap to prevent further ionization. However, in the future, we will want to make this process computer-controllable. We have left space in the optical breadboard design for 375/423 nm (Figure 3.5a) for a shutter. Additionally, we will want similar computer controllable shutters for the beams going to wavemeters, so we can control which beam frequencies are measured.

5.1.4 O_2 Lasers

Additionally, we will need to propagate the lasers for O_2 transitions into the trap. These transitions include the state-selective photo-ionization transition via a 2+1 resonance-enhanced multi-photon ionization (REMPI) through a 301 nm pulsed laser, the vibrational transition via a 767.6 nm ECDL, and a dissociation beam of 355 nm in order to detect a successful vibrational transition. The Hanneke Lab has already successfully prepared $^{16}O_2^+$ in the trap using the 2+1 REMPI technique [56]. Realigning that beam, which will also propagate at 45° from the trap's axis, will allow us to co-trap $^{16}O_2^+$ and $^{40}Ca^+$. Then, we can begin setting up the 767.7 nm ECDL, which will propagate along the trap's axis in a Fabry-Perot cavity, building up power. Finally, we can apply the dissociation beam of 355 nm in order to break the chemical bond.

5.2 Measuring $\dot{\mu}$

In order to test for the vibrational frequency of $^{16}O_2^+$, we apply AC modulation to our electrodes at lower frequencies and voltages than the RF signal, which allows us to measure the

secular frequencies of the trapped particles. When the modulation equals the secular frequencies of the trapped particles, this system is essentially like driving a harmonic oscillator at the resonance frequency, which increases the amplitude of oscillations. This will cause an already cooled Coulomb crystal to laser cool at a much lower rate, lose its shape, and fluoresce much less. This is called a "tickle" experiment. We can confirm that we successfully drove the $v = 0$ to $v = 16$ vibrational transition if we are able to tickle our crystal at a frequency where we expect an O^+ atom to be tickled. This is because the dissociation laser only breaks the chemical bond of $^{16}O_2^+$ if we successfully drove the $v = 0$ to $v = 16$ vibrational transition. From there, we can measure the frequency used to drive the transition from $v = 0$ to $v = 16$. Repeating this experiment over the course of a year will allow us to probe for drifts in μ, as explained in Section 1.4.

5.3 Other Considerations

Certain questions still remained unanswered, such as the geometric factor κ's dependence on DC well configurations. It has been previously found that the measurement of axial frequency using the tickling techniques described in Section 5.2 is heavily dependent on the amplitude of the AC modulation [26]. The geometric factor κ can therefore be better understood and measured using a variety of amplitudes for the AC drive.

We also used a variety of laser powers for the transitions of ^{40}Ca, as stated in Section 4.2. However, those laser powers are not necessarily the most efficient for loading ions. Calculations can be made and tested in order to optimize the loading of $^{40}Ca^+$.

It is also important to be able to get the ion trap vacuum chamber down to 10^{-10} Torr during experiments, which we were unable to do when we loaded the calcium crystals. An important next step is troubleshooting this issue, so that we can load $^{40}Ca^+$ and $^{16}O_2^+$ in ideal vacuum chamber conditions.

5.4 Applications of These Techniques

As stated in Chapter 1, the theory and techniques used in this project have strong applications in quantum computing, where trapped ions have long been strong candidates for qubits. Calcium, in particular, is not an uncommon choice for a qubit. However, to achieve the *omg* architecture, as described in Section 1.2.2, a magnetic field would be required to create the Zeeman splittings. This would allow for the ground state and metastable state qubits to exist. From here, we have a few options for preparing quantum states, performing gates, storing, and reading out.

Figure 5.1 demonstrates the transitions for a possible scheme for state preparation and gate operation for $^{40}Ca^{+}$. First, trap an ion crystal with all ions initially in the ground state, $4S_{1/2}$. Target ions would be driven to the $3D_{5/2}$ states via a 729 nm laser, while coolant ions are Doppler cooled via the 397 nm and 866 nm beams. The gates can then be completed with global beams, meaning the laser does not have be focused on a single ion and can hit all ions in the scheme. Since the target ions are in the $3D_{5/2}$ manifold, they will be unaffected by 397 nm and 866 nm beams, but they are sympathetically cooled by the other ions. On the target ions (or data qubits), we can perform a 2-qubit-gate by choosing two target ions and performing a Raman transition between the $3D_{5/2}$ and the $4P_{3/2}$ states. A Raman transition is a 2 photon transition slightly detuned to prevent populating the $4P_{3/2}$ state. It is not necessary to know the inner workings of this process for this discussion, but it is an example of performing an operation (manipulating the quantum state) on the target ions with high fidelity [7]. From there, the target ions are coherently transfered back to the ground state for storage [8]. Then, we can coherently transfer all ions except the target ions to the metastable state, shelving them, and converting the stored target ions into the optical qubits for detection [8]. In most scenarios, read out involves the process described in Section 1.2.1, encoding the target ions into the state coupled to a cycling transition and a state not coupled to the cycling transition.

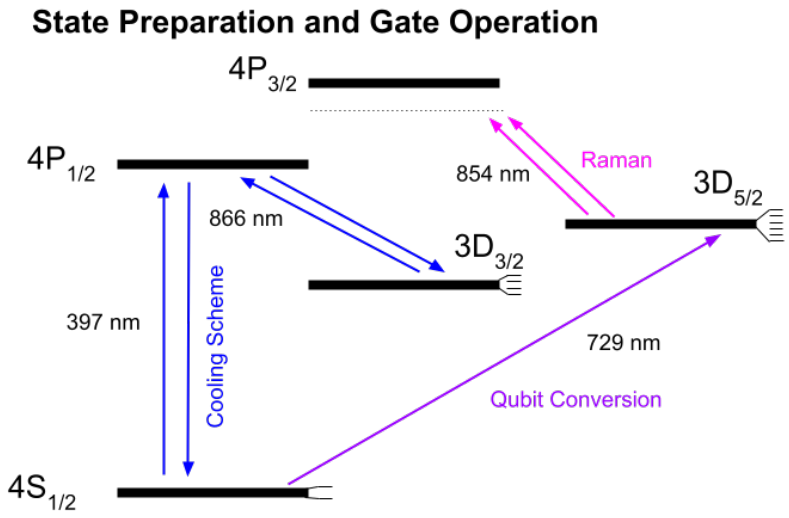

Figure 5.1: Simplified scheme of state preparation and gate operation. We can prepare the states by driving the target ions to the $3D_{5/2}$ state and cool the remaining ions via the 397 nm and 866 nm transitions. From there, we can perform gate operations on the ions in the $3D_{5/2}$ manifold. In this figure, we show a 2-qubit-gate operation in the form of a Raman transition and 854 nm light.

5.5 Final Remarks

This thesis project is built towards a dual-species scheme, which is inherently contradictory to the discussion of the *omg* architecture. We do not apply a magnetic field to our ions, nor do we have a 729 nm or a 854 nm laser. However, trapped-ion quantum computing uses the same principles as we do, as well some of the same tricks. Some new tricks used in trapped-ion quantum computing might eventually be used in the Hanneke Lab. Trapped-ion quantum computing provides a component of my personal motivation for ion-trapping work, but my overall motivation for the project is rooted in the journey of the Hanneke Lab.

In conclusion, this project is only a step in the right direction towards a much larger goal for the Hanneke Lab: testing for time variation in μ. It was built on the foundation of hard work from Professor Hanneke, previous undergraduate projects, thesis projects, and postdoctoral research. This thesis project was not the first step in the journey towards this goal, and it certainly will not be the last. There is much more work to be done. However, the end goal is not too far away. The Hanneke Lab now has the major equipment to search for the $^{16}O_2^+$ vibrational line. I am very excited to see where future lab projects and theses take this search.

Appendix A

The Calcium Oven

One of the key aspects of making the switch to sympatheically cool $^{16}O^+$ with $^{40}Ca^+$ is getting calcium into the trap. In the past, we introduced beryllium into the trap with an oven that consisted of a tungsten wire wrapped with beryllium wire. Running current through them until the wires turn orange hot increased the vapor pressure of beryllium. Getting calcium into the trap required the construction of a new oven to replace one of the old beryllium ovens. We took inspiration from other lab groups, who built their oven similarly to how we did for our new calcium oven [37, 57–59]. In the end, the calcium oven is a stainless steel tube, crimped on both sides, with a small hole cut in the side, and full of calcium granules. Similar to the beryllium oven, we run a current through the assembly, which heats up the calcium. This increases the vapor pressure of calcium, which then escapes through the hole.

A.1 Oven Construction

Through consultation with [37, 57–59] and trial and error, we found the following steps to be most successful for building calcium ovens:

1. Cut a stainless steel tube of outer diameter 0.072" and wall thickness 0.005" (McMaster Part 89935K56) into approximately 20 mm increments.

2. Crimp about 5 mm of tubing from the end of the tube until flat. Fold that 5 mm in half so that there is now a 2.5 mm long, doubled-crimped bottom, which is helping for welding.

3. Using a thin handsaw, create a slit about 3mm away from where the double crimp ends. This slit is where calcium will exit the tube into the trap. Deburr inside of tubing using molybdenum wire.

4. In a nitrogen bag, insert 12-20 calcium granules using clean tools. It must be done in a nitrogen bag, as calcium oxidizes if exposed to air for too long. We found that we comfortably have an hour in air before there is noticeable oxidation.

5. Crimp the tubing closed on the other side. This crimp is 9 mm long. Similarly, fold this into a 4.5 mm double crimp.

6. Weld.

The length of the oven tubing ended as approximately 6 mm long. The first five steps in Figure A.1 illustrates this process.

A.2 Welding

Electrical connections were needed to be made so that we could run current through the oven and insert the oven into the oven mount. One end of the oven needed to be welded to molybdenum wire, and the other needed to be welded to a constantan ribbon (for ground). To weld the oven and the electrical connections together, we followed the following procedure:

1. With the Miller Electric MSW-41T spot welder, use 12-inch copper electrodes. To add more resistance to the system, and an additional 6-inch extension, which also allows us to use small electrode tips. We attached Amada Tech ES0813: 2" height, 1/4" body diameter, and 3/32" diameter tungsten electrode tips.

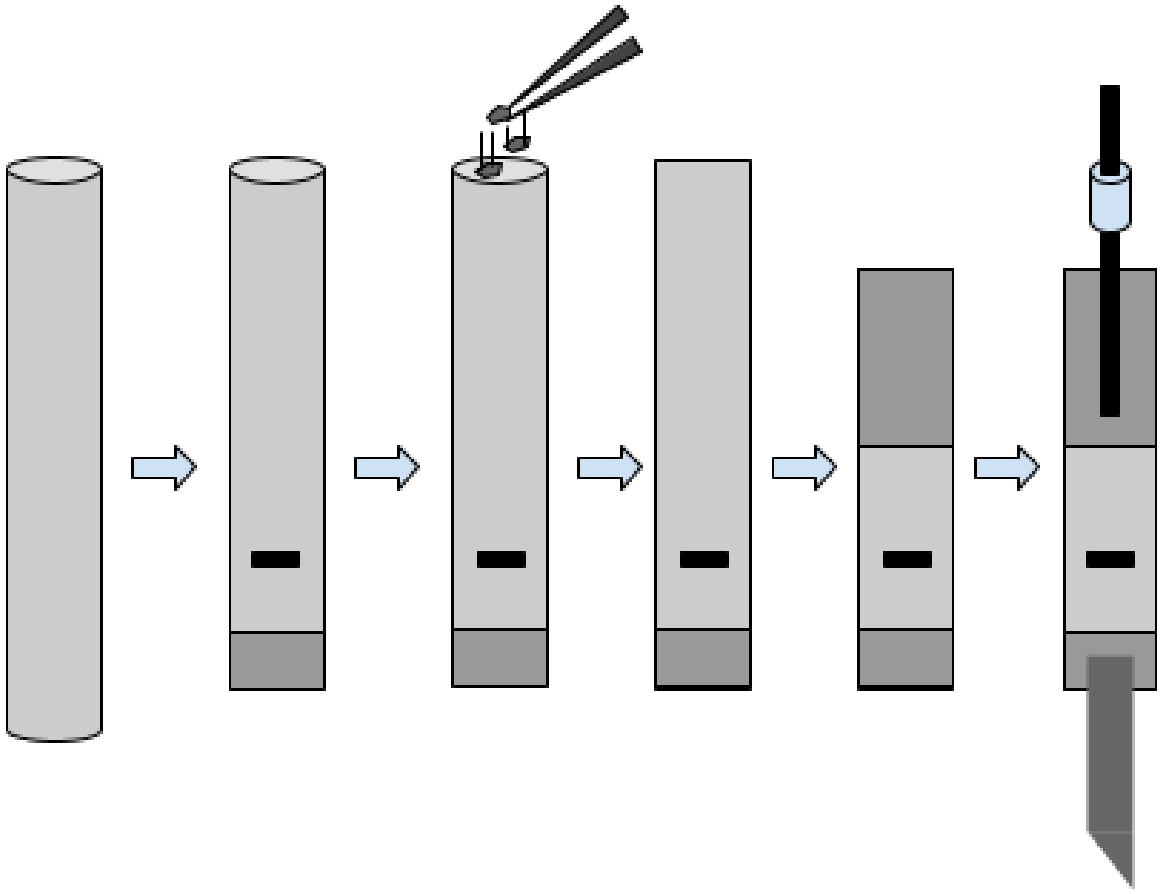

Figure A.1: Steps to have oven ready for insertion into trap. Please note that in the mount, the oven will actually be the flipped version of what this figure shows.

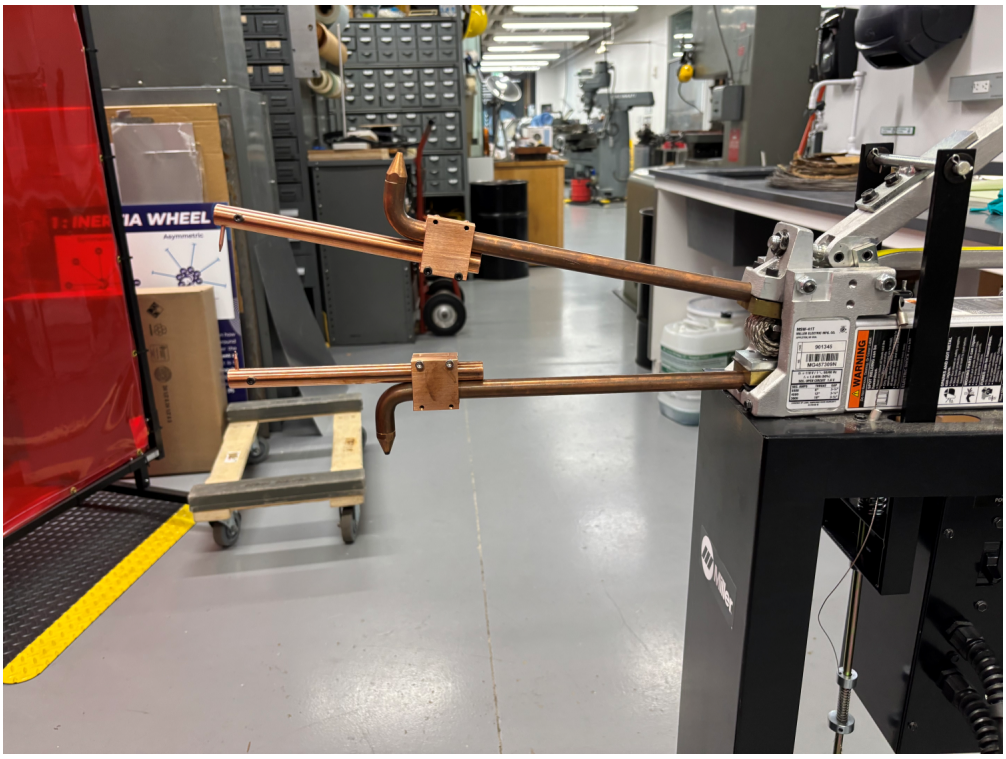

Figure A.2: The Miller Electric MSW-41T spot welder, with 12-inch copper electrodes, additional 6-inch extension, and Amada Tech ES0813 tungsten electrode tips.

2. Before welding, adjust electrode tips by hand so that they are lined up flat with one another. Let go and hold the two materials tightly via a pedal (part of the spot welder system).

3. Adjust current setting on welder to just above the .10 s setting. Weld molybdenum wire to the longer, 7 mm long double-crimped part of the tube. This serves as the bottom connection in the oven mount.

4. Adjust current setting on welder to just above the .05 s setting. Weld the constantan ribbon to the shorter, 2.5 mm long double-crimped part of the tube. This serves as the ground connection at the top of the oven mount.

5. Store welded ovens in a vaccuum.

A.3 Installation

The previous set-up for beryllium and oxygen dual-species trapping introduced beryllium using one of two available ovens. We replaced one of the beryllium ovens with a calcium oven built in Sections A.1 and A.2. To install the oven, we followed the following steps:

1. Ease the vacuum chamber containing the trap to atmospheric pressure by closing the gate valves to maintain a rough vacuum in the oxygen beam chambers, turning off the ion pump, and venting nitrogen.

2. Loosen the screws on the top and bottom trap flanges. The oven mount and the trap plate itself are attached to the bottom flange.

3. Remove the screws and slowly lower bottom trap flange from trap chamber. Repeat same process with top flange.

4. Unscrew the oven mount from the trap plate, leaving it to dangle from its wire connections in the trap.

5. Remove a beryllium oven by loosening the screw holding the oven in place.

6. Remove the calcium oven from its separate vacuum chamber, install it, and adjust its position to align the slit in the stainless steel with the center of the trap.

7. Place a copper gasket onto the trap plate to ensure a vacuum seal. Since we are making electrical connections inside the chamber, it is essential to do this before mounting the oven mount back onto the trap plate. Otherwise, we would encounter a topological issue when attempting to raise the bottom flange back to the main trap chamber.

8. Mount the oven mount onto the trap plate.

9. Raise the trap plate back into the main chamber and screw it in place using the star pattern.

10. Flow nitrogen through the chamber, which still has its top viewport flange open. This allows us to adjust wires to ensure beam clearance.

11. With a new copper gasket, tighten the top flange to the top of the main trap chamber.

12. With all flanges on and screwed in, stop flowing nitrogen, connect the vacuum pump and a Residual Gas Analyzer, and begin pumping.

A.4 Oven Tests

To ensure the calcium oven functions properly, we conducted two tests. They verified that our oven was not electrically shorted in the trap and that it could reach a sufficiently high temperature to introduce calcium into the trap chamber.

1. Run current through the oven until we could see the oven glow with an infrared viewer. If the oven glows, then it means that the oven is not shorted.

2. While running current through the oven, direct a 423 nm laser into the chamber and see if we can see fluorescence from exciting the calcium from its 4S to 4P state. If we observe fluorescence, it means that our ovens are releasing calcium into the trap chamber.

Since our pins were only rated to 5 A, we used two pins and a 2-1 connection to increase the max current to 10 A. This required rewiring on the vacuum side and air side. We first observed fluorescence when running 8.2 A through the oven, but it was also visible later at 6.2 A. We suspect this is because calcium developed an oxide layer when it was being installed into the trap from the room air. It took more current to heat up the granules to initially diffuse the oxide layer than it does to increase the vapor pressure of the calcium granules to the point where atoms escape. When we load ions, our routine currents are about 6 A.

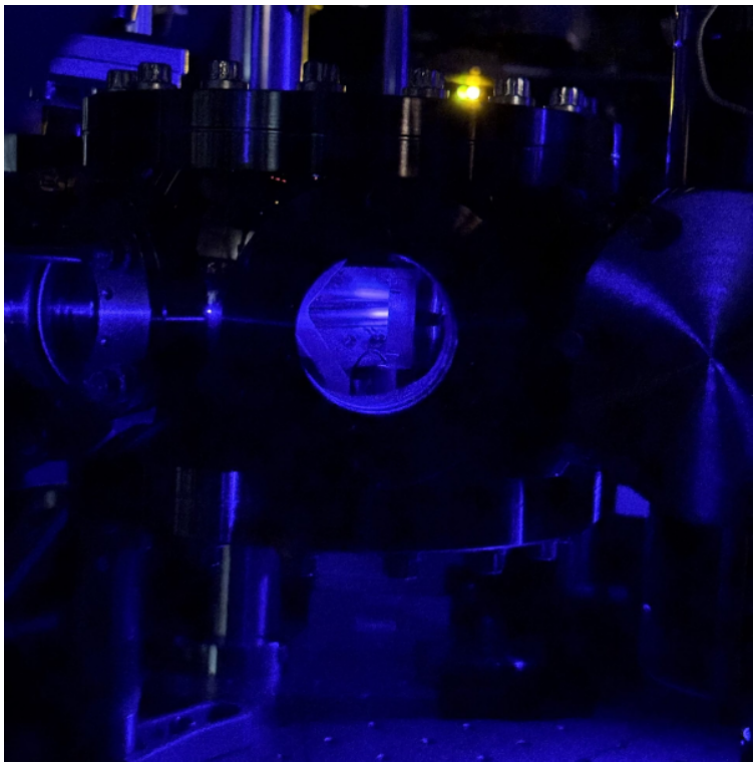

Figure A.3: View of trap chamber with a view port showing the 423 nm beam fluoresce ^{40}Ca.

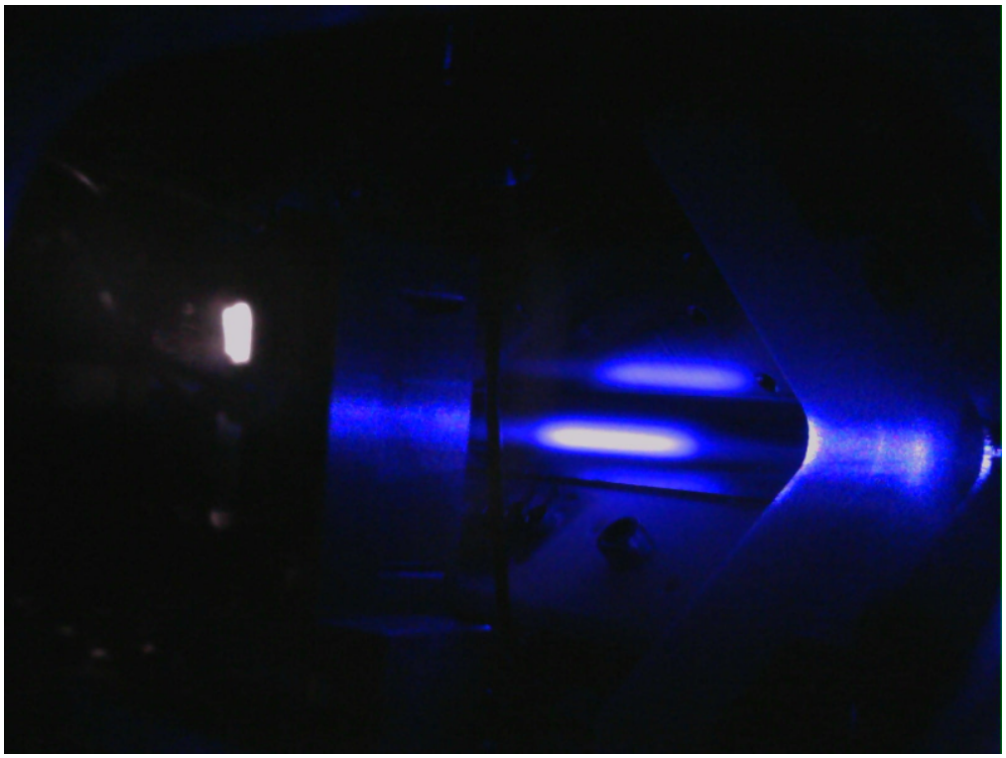

Figure A.4: The full view through another viewport, where we can see the glowing of the calcium oven, two trap electrodes, and a cloud of ^{40}Ca fluorescing.

Appendix B

Anamorphic Prism Pair

In order to circularize the 866 nm beam shape, we decided to orient an anamorphic prism pair at $\alpha_1 = 31^\circ$ and $\alpha_2 = 0^\circ$ to obtain a magnification of 3.4 ± 0.1. Since the prisms were unmounted, James Kubasek helped us machine a mount where the prisms could be placed at the desired angles. From there, we used epoxy to cement the prisms in place. The SolidWorks drawing is represented in Figure B.1, and a photo of the mount with the prisms is represented in Figure B.2.

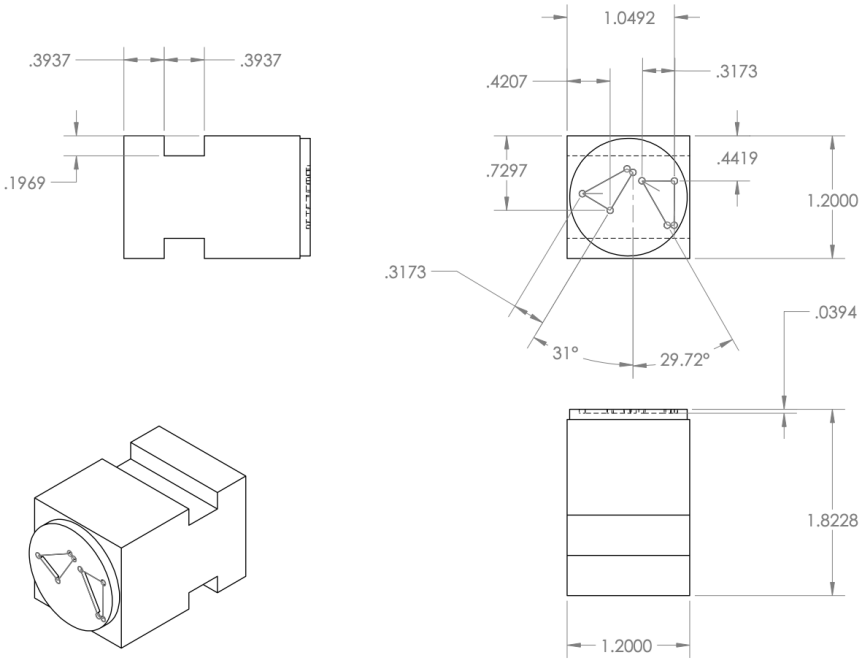

Figure B.1: SolidWorks Drawing of Prism Mount. Credit to James Kubasek

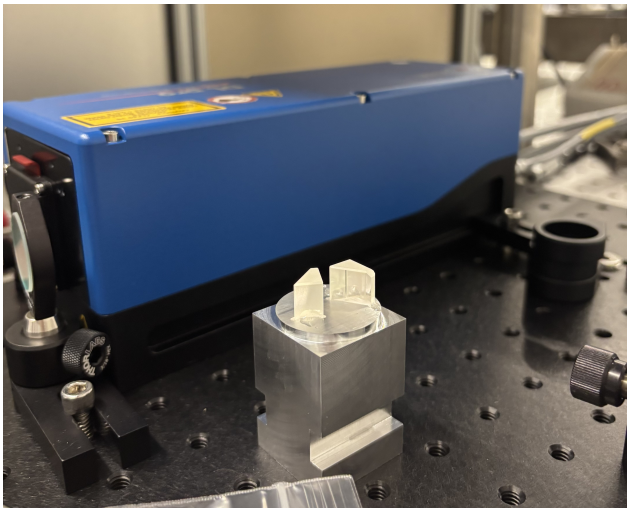

Figure B.2: Anamorphic prism pair oriented at the desired angles. From here, the mount could bolted to the breadboard.

Bibliography

[1] W. Paul, "Electromagnetic traps for charged and neutral particles," **62**, 531 (1990).

[2] A. Y. Kitaev, A. Shen, and M. N. Vyalyi, *Classical and quantum computation*, 47 (American Mathematical Soc., 2002).

[3] C. Hughes, J. Isaacson, A. Perry, R. F. Sun, and J. Turner, *Quantum Computing for the Quantum Curious* (Springer International Publishing, Cham, 2021), ISBN 978-3-030-61600-7, URL http://link.springer.com/10.1007/978-3-030-61601-4.

[4] R. P. Feynman, "Quantum Mechanical Computers," Optics News **11**, 11 (1985).

[5] G. Werth, V. N. Gheorghe, and F. G. Major, *Charged Particle Traps II: Applications*, Springer Series on Atomic, Optical, and Plasma Physics (Springer-Verlag Berlin Heidelberg, 2009).

[6] D. P. DiVincenzo, "The Physical Implementation of Quantum Computation," Fortschritte der Physik **48**, 771–783 (2000), ISSN 1521-3978, URL http://dx.doi.org/10.1002/1521-3978(200009)48:9/11<771::AID-PROP771>3.0.CO;2-E.

[7] C. D. Bruzewicz, J. Chiaverini, R. McConnell, and J. M. Sage, "Trapped-Ion Quantum Computing: Progress and Challenges," Applied Physics Reviews **6**, 021314 (2019).

[8] D. T. C. Allcock, W. C. Campbell, J. Chiaverini, I. L. Chuang, E. R. Hudson, I. D. Moore, A. Ransford, C. Roman, J. M. Sage, and D. J. Wineland, "omg blueprint for

trapped ion quantum computing with metastable states," Applied Physics Letters **119** (2021), ISSN 1077-3118, URL http://dx.doi.org/10.1063/5.0069544.

[9] W. Demtröder, *Atoms, Molecules and Photons: An Introduction to Atomic-, Molecular- and Quantum Physics*, Graduate Texts in Physics (Springer, 2018), 3rd ed., ISBN 978-3-662-55521-7.

[10] A. D. Ludlow, M. M. Boyd, J. Ye, E. Peik, and P. O. Schmidt, "Optical atomic clocks," Rev. Mod. Phys. **87**, 637 (2015), URL https://link.aps.org/doi/10.1103/RevModPhys.87.637.

[11] National Institute of Standards and Technology, "Second: The Present," https://www.nist.gov/si-redefinition/second-present (2026).

[12] M. S. Safronova, D. Budker, D. DeMille, D. F. Jackson Kimball, A. Derevianko, and C. W. Clark, "Search for new physics with atoms and molecules," **90**, 025008 (2018).

[13] J.-P. Uzan, "The stability of fundamental constants," Comptes Rendus. Physique **16**, 576 (2015).

[14] R. Gambini and J. Pullin, "Discrete Quantum Gravity: A Mechanism For Selecting The Value of Fundamental Constants," International Journal of Modern Physics D **12**, 1775 (2003).

[15] D. Hanneke, B. Kuzhan, and A. Lunstad, "Optical clocks based on molecular vibrations as probes of variation of the proton-to-electron mass ratio," **6**, 014005 (2021).

[16] J.-P. Uzan, "Varying Constants, Gravitation and Cosmology," Living Rev. Relativity **14**, 2 (2011).

[17] R. Carollo, A. Frenett, and D. Hanneke, "Two-Photon Vibrational Transitions in $^{16}O_2^+$ as Probes of Variation of the Proton-to-Electron Mass Ratio," Atoms **7**, 1 (2018), URL https://doi.org.

[18] A. Lunstad, "Driving Forbidden Vibrational Transitions in Molecular Oxygen," (2021), Undergraduate Honors Thesis, Amherst College, Amherst, Massachusetts.

[19] D. J. Griffiths, *Introduction to Electrodynamics* (Cambridge University Press, 2023), 5th ed., ISBN 978-1-009-39775-9.

[20] S. Qiao, "Constructing a Linear Paul Trap System for Measuring Time-Variation of the Electron-Proton Mass Ratio," (2013), Undergraduate Honors Thesis, Amherst College, Amherst, Massachusetts.

[21] D. A. Lane, "Developing a Quantum Toolbox: Experiments with a Single-Atom Harmonic Oscillator and Prospects for Probing Molecular Ions," (2017), Undergraduate Honors Thesis, Amherst College, Amherst, Massachusetts.

[22] M. G. Raizen, J. M. Gilligan, J. C. Bergquist, W. M. Itano, and D. J. Wineland, "Ionic crystals in a linear Paul trap," Phys. Rev. A **45**, 6493 (1992), URL `https://link.aps.org/doi/10.1103/PhysRevA.45.6493`.

[23] M. Abramowitz and I. A. Stegun, *Handbook of Mathematical Functions* (National Bureau of Standards, 1972).

[24] N. W. McLachlan, *Theory and Application of Mathieu Functions* (Clarendon Press, Oxford, 1947).

[25] D. Leibfried, R. Blatt, C. Monroe, and D. Wineland, "Quantum dynamics of single trapped ions," Rev. Mod. Phys. **75**, 281 (2003), URL `https://link.aps.org/doi/10.1103/RevModPhys.75.281`.

[26] W. Henshon, "Radiofrequency circuit design for ion trapping of O_2 molecules," (2022), Undergraduate Honors Thesis, Amherst College, Amherst, Massachusetts.

[27] G. F. Weston, *Ultrahigh Vacuum Practice* (Butterworths, London ; Boston, 1985), ISBN 978-0-408-01485-4, 288 pages.

[28] Morgan Advanced Materials, "MACOR Machinable Glass Ceramic," (2026), https://www.morgantechnicalceramics.com/en-gb/products/macor-machinable-glass-ceramic/.

[29] Leybold, *TURBOVAC 90 iX - Technical Data - DN 63 ISO-K*, Leybold (2026), URL https://www.leyboldproducts.us/media/pdf/69/d3/d0/TD_810031V3300_EN.pdf.

[30] Stanford Research Systems, *Models RGA100, RGA200, and RGA300 Residual Gas Analyzer Operation and Service Manual*, Stanford Research Systems (2015), available at: https://www.thinksrs.com/downloads/pdfs/manuals/RGA120m.pdf.

[31] D. J. Wineland and W. M. Itano, "Laser cooling of atoms," Phys. Rev. A **20**, 1521 (1979), URL https://link.aps.org/doi/10.1103/PhysRevA.20.1521.

[32] N. Bohr, "On the constitution of atoms and molecules," Philosophical Magazine **26**, 1 (1913).

[33] M. Baldo, "The dynamics of spontaneous emission," (2025), 2505.22164, URL https://arxiv.org/abs/2505.22164.

[34] F. Diedrich, E. Peik, J. M. Chen, W. Quint, and H. Walther, "Observation of a Phase Transition of Stored Laser-Cooled Ions," Phys. Rev. Lett. **59**, 2931 (1987), URL https://link.aps.org/doi/10.1103/PhysRevLett.59.2931.

[35] B. Roth, U. Fröhlich, and S. Schiller, "Sympathetic Cooling of $^4He^+$ Ions in a Radio-Frequency Trap," Phys. Rev. Lett. **94**, 053001 (2005), URL https://link.aps.org/doi/10.1103/PhysRevLett.94.053001.

[36] U. Becker and D. A. Shirley, *VUV and Soft X-Ray Photoionization*, Physics of Atoms and Molecules (Plenum Press, New York, 1996), ISBN 0-306-45038-0.

[37] D. M. Lucas, A. Ramos, J. P. Home, M. J. McDonnell, S. Nakayama, J.-P. Stacey, S. C. Webster, D. N. Stacey, and A. M. Steane, "Isotope-selective photoionization for calcium

ion trapping," Phys. Rev. A **69**, 012711 (2004), URL https://link.aps.org/doi/10.1103/PhysRevA.69.012711.

[38] C. C. Teng, "Frequency Control and Stabilization of a Laser System," (2013), Undergraduate Honors Thesis, Amherst College, Amherst, Massachusetts.

[39] B. E. A. Saleh and M. C. Teich, *Fundamentals of Photonics*, Wiley Series in Pure and Applied Optics (John Wiley & Sons, Hoboken, New Jersey, 2019), 3rd ed., Part 2: Photonics.

[40] Y. Wang and Y. Song, "Recent Advances in Tunable External Cavity Diode Lasers," Applied Sciences **15**, 206 (2024).

[41] Edmund Optics, Inc., "Anamorphic Prism Pairs," (2026), accessed: 2026-03-30, URL https://www.edmundoptics.com/knowledge-center/application-notes/optics/anamorphic-prism-pairs/?srsltid=AfmBOorTjjlbUjO_usUidrQRpk6IOdOM-Q2OhzeJeu5uCI3R0tbLVRNS.

[42] Thorlabs, Inc., "Anamorphic Prism Pairs," (2026), accessed: 2026-03-30, URL https://www.thorlabs.com/anamorphic-prism-pairs?tabName=Collimation%20Tutorial.

[43] B. E. A. Saleh and M. C. Teich, *Fundamentals of Photonics*, Wiley Series in Pure and Applied Optics (John Wiley & Sons, Hoboken, New Jersey, 2019), 3rd ed., Part 1: Optics.

[44] Thorlabs, Inc., "Broadband Polarizing Beamsplitter Cubes," (2026), URL https://www.thorlabs.com/broadband-polarizing-beamsplitter-cubes?tabName=Overview.

[45] Edmund Optics, Inc., "400nm, 12.5mm Diameter, Dichroic Longpass Fil-

ter," (2026), accessed: 2026-03-30, URL https://www.edmundoptics.com/p/400nm-125mm-diameter-dichroic-longpass-filter/24130/.

[46] E. A. Donley, T. P. Heavner, F. Levi, M. O. Tataw, and S. R. Jefferts, "Double-pass acousto-optic modulator system," Review of Scientific Instruments **76**, 063112 (2005), URL https://doi.org/10.1063/1.1930095.

[47] Thorlabs, Inc., "Beam Expander Design Comparison: Keplerian and Galilean," (2026), accessed: 2026-04-01, URL https://www.thorlabs.com/beam-expander-design-comparison-keplerian-and-galilean?tabName=Insights.

[48] R. S. Quimby, *Cylindrical Waveguides* (John Wiley Sons, Ltd, 2006), chap. 4, pp. 43–54, ISBN 9780471791591, https://onlinelibrary.wiley.com/doi/pdf/10.1002/0471791598.ch4, URL https://onlinelibrary.wiley.com/doi/abs/10.1002/0471791598.ch4.

[49] Thorlabs, Inc., "Single Mode FC/PC Fiber Optic Patch Cables," (2026), URL https://www.thorlabs.com/single-mode-fcpc-fiber-optic-patch-cables?tabName=Insights.

[50] S. C. Doret, "Simple, low-noise piezo driver with feed-forward for broad tuning of external cavity diode lasers," Review of Scientific Instruments **89** (2018), ISSN 1089-7623, URL http://dx.doi.org/10.1063/1.5009643.

[51] National Institute of Standards and Technology, "Atomic Spectra Database," https://https://www.nist.gov/pml/atomic-spectra-database (2026).

[52] H. Wu, M. Mills, E. West, M. C. Heaven, and E. R. Hudson, "Increase of the barium ion-trap lifetime via photodissociation," Phys. Rev. A **104**, 063103 (2021), URL https://link.aps.org/doi/10.1103/PhysRevA.104.063103.

[53] L. Duca, N. Mizukami, E. Perego, M. Inguscio, and C. Sias, "Orientational Melting in a Mesoscopic System of Charged Particles," Phys. Rev. Lett. **131**, 083602 (2023), URL https://link.aps.org/doi/10.1103/PhysRevLett.131.083602.

[54] B. V. Pashinsky, A. Kato, and B. B. Blinov, "Structural Transitions and Melting of Two-Dimensional Ion Crystals in RF Traps," Entropy **27**, 325 (2025), URL https://www.mdpi.com/1099-4300/27/4/325.

[55] Y. V. Stadnik and V. V. Flambaum, "Can Dark Matter Induce Cosmological Evolution of the Fundamental Constants of Nature?" Phys. Rev. Lett. **115**, 201301 (2015), URL https://link.aps.org/doi/10.1103/PhysRevLett.115.201301.

[56] A. P. Singh, M. Mitchell, W. Henshon, A. Hartman, A. Lunstad, B. Kuzhan, and D. Hanneke, "State selective preparation and nondestructive detection of trapped O2+," The Journal of Chemical Physics **162** (2025), ISSN 1089-7690, URL http://dx.doi.org/10.1063/5.0244447.

[57] R. B. Blakestad, *Transport of Trapped-Ion Qubits within a Scalable Quantum Processor*, PhD Thesis, University of Colorado (2010).

[58] S. A. Schulz, *Scalable Microchip Ion Traps for Quantum Computation*, Doctoral dissertation, University of Ulm (2009).

[59] A. D. Quinn, *Novel entangling gates and scalable trap designs for trapped-ion quantum computing*, Doctoral dissertation, University of Oregon, Eugene, OR, USA (2024), URL https://inspirehep.net/authors/2676554.